# *High-Volume-Fraction Textured Carbon Nanotube-Bis(maleimide) and -Epoxy Matrix Polymer Nanocomposites: Implications for High-Performance Structural Composites*

# High Volume Fraction Textured Carbon Nanotube-Bismaleimide and -Epoxy Matrix Polymer Nanocomposites: Implications for High-Performance Structural Composites

Ashley L. Kaiser,[*,†] Cécile A. C. Chazot,[†,‡] Luiz H. Acauan,[¶] Isabel V. Albelo,[¶,§] Jeonyoon Lee,[¶] Jeffrey L. Gair Jr.,[¶,‖,⊥,#] A. John Hart,[‡] Itai Y. Stein,[¶] and Brian L. Wardle[*,¶,‡]

†*Department of Materials Science and Engineering, Massachusetts Institute of Technology, Cambridge, MA 02139, USA.*

‡*Department of Mechanical Engineering, Massachusetts Institute of Technology, Cambridge, MA 02139, USA.*

¶*Department of Aeronautics and Astronautics, Massachusetts Institute of Technology, Cambridge, MA 02139, USA.*

§*Department of Materials Science and Engineering, University of California, San Diego, La Jolla, CA 92093, USA.*

‖*Scinetics, Inc, 2915 Islay Court, Abingdon, MD 21009, USA.*

⊥*Institute for Soldier Nanotechnologies, Cambridge, MA 02139, USA.*

#*U.S. Army Research Laboratory, RDRL-VTM, Aberdeen Proving Ground, MD 21005, USA.*

E-mail: alkaiser@alum.mit.edu; wardle@mit.edu

**Abstract**

Polymer matrix nanocomposites (PNCs) incorporating high volume fractions ($V_f$ in excess of 10 vol%) of aligned carbon nanotubes (A-CNTs) are promising for high-performance structural composite applications leveraging texture for multifunctionality and performance-to-weight ratios. However, to enable manufacturing of scalable structures using A-CNT PNCs, nanoscale confinement and interfacial effects due to high A-CNT content in aerospace-grade polymer matrices need to be better understood. Here, we report model-informed fabrication of high CNT $V_f$ PNCs to develop process-structure-property relationships, including a scaled film and laminate technique for A-CNT polymer laminates, and the fabrication of microvoid-free and fully infused bismaleimide (BMI) and epoxy PNCs with high packing densities (volume fractions) of biaxially mechanically densified mm-tall A-CNT array reinforcement (1 to 30 vol%, corresponding to average inter-CNT spacings of ∼70 to 6 nm). A polymer infusion model developed from Darcy's law accurately predicts the time for resin to infuse into CNT arrays during capillary-assisted PNC processing, corroborated by experimental observations *via* X-ray micro-computed tomography and scanning electron microscopy that a diluted resin with ∼10 × lower viscosity than neat resin is required to obtain complete infusion into high CNT $V_f$ A-CNT arrays (10−30 vol%). For each tested A-CNT vol%, the cured PNCs maintain vertical CNT alignment and glass transition temperature, and the decomposition onset temperature remains constant for epoxy PNCs but increases by ∼8°C for 30 vol% A-CNT BMI PNCs compared to the neat resin. For both polymer matrix systems, a ∼2 × increase in the axial indentation modulus for 30 vol% A-CNT PNCs compared to neat resin is measured, and no significant change in transverse A-CNT modulus is shown experimentally and *via* modeling, indicating that reinforcement with A-CNTs at higher $V_f$ leads to enhanced anisotropic mechanical properties. Through the process-structure-property scaling relations established here, this work is envisioned to support the development of next-generation structures comprised of nanomaterials with enhanced performance and manufacturability.

Keywords: carbon nanotubes, high performance structural composites, thermoset resin, infusion model, nanoscale confinement

# Introduction

Recent work highlighting novel one-dimensional (1D) nanoscale systems, such as those based on aligned nanofibers,[1,2] provides exciting opportunities for the fabrication of high-performance nanomaterials and devices.[3,4] Specifically, the advantaged mass-specific thermal, electrical, and mechanical characteristics of aligned carbon nanotubes (A-CNTs)[2] make them favorable for next-generation composites and commercial applications in a variety of industries, especially with new nanoscale technologies leveraging multifunctionality.[5,6] The performance of such products, particularly aerospace composites and advanced hybrid laminates, may be enhanced when A-CNTs are used in high fiber volume fractions, commonly vol%, $V_f$, to fabricate lightweight materials with improved stiffness, toughness, electrical and thermal conductivity, and thermal stability,[7–10] as shown by a ∼1800% and ∼800% increase in thermal conductivity over the matrix for 20 vol% CNT-epoxy composites in the axial and transverse CNT directions, respectively,[10] a ∼9000% increase in effective axial elastic modulus for 1 to 20 vol% A-CNT arrays,[8,11] and a ∼400% increase in electrical conductivity for 20 vol% A-CNT/epoxy composites as compared to 1 vol% randomly oriented CNT/epoxy composites.[12] Many prior studies have focused on relatively low CNT reinforcement (*e.g.* 1 vol% or less) in polymer matrix nanocomposites (PNCs),[13,14] where CNT incorporation in the matrix often does not significantly improve properties, even with good CNT dispersion,[14] and CNT functionalization/resin modifications are often required to improve performance, such as the impact strength at low CNT loadings.[14] In contrast, this study describes process-structure-property relations for PNCs with up to 30 vol% A-CNTs to explore further improvements that can be achieved at high loadings with neat resin, here demonstrating the successful fabrication and enhanced performance of highly packed CNT-polymer composite systems for high-performance structural composites, *e.g.* in aerospace applications.

CNTs have been used to reinforce polymer matrix nanocomposites (PNCs) in both aligned[9,15] and randomly oriented CNT morphologies,[16] where alignment takes primary advantage of the anisotropic physical properties of CNTs[1] while facilitating the polymer infu-

sion process during PNC fabrication through the capillary-assisted wetting of aligned CNTs with a polymer matrix.[7,12,17] Maintaining CNT alignment while increasing CNT $V_f$ *via* mechanical densification enhances processing and performance at the bulk structural level, as highlighted by previous studies leveraging vertical CNT alignment to facilitate epoxy resin infusion into A-CNT arrays up to ∼20 vol% CNT $V_f$.[7,12] However, past work also underscores the need for greater mechanistic understanding of the main processing factors that ultimately tailor composite performance, such as resin viscosity, surface energy, CNT geometry, density, and alignment in the polymer matrix. These often govern the physical and chemical CNT-polymer interactions observed experimentally[18] and through recent CNT-polymer molecular modeling studies.[19,20] These factors are even more critical when CNT $V_f$ increases to yield nm-scale (1-10 nm) inter-CNT spacings on the order of the radius of gyration for polymers such as epoxy and BMI resins (∼3−30 nm)[7,21] at A-CNT volume fractions of ∼20 vol% and higher. Therefore, it is necessary to understand how high CNT $V_f$ affects polymer infusion limits during PNC fabrication, and likewise how polymer confinement in high vol% A-CNT arrays influences the structure, morphology, interfacial effects, and thermal and mechanical behavior of PNCs at fixed CNT heights and representative volumes, as shown in Figure 1, including extension to novel bulk nanocomposite laminates introduced here for the first time.

It is well known that interfacial interactions can dominate the mechanical and thermal behavior of composites even at low CNT $V_f$ (∼1 vol% as-grown A-CNTs with ∼70 nm inter-CNT spacings),[22] and particularly as the CNT $V_f$ increases, such as for densified 30 vol% A-CNT arrays with ∼6 nm inter-CNT spacings.[8,11,22,23] In these cases, the interfacial surface area to volume ratio is large (*i.e.* ∼700× larger for a typical 10 nm diameter CNT compared to a 7 μm diameter carbon fiber, both at 60 vol% in a composite), the interphase region can extend 1−100 nm from the CNT surface depending on the polymer,[18,24] and the inter-CNT spacing is small and on the order of the radius of gyration for polymers (3−30 nm), which therefore has the potential to alter polymer behavior such as polymer chain mobility, crystallinity, glass transition temperature ($T_g$), and curing.[25] For example,

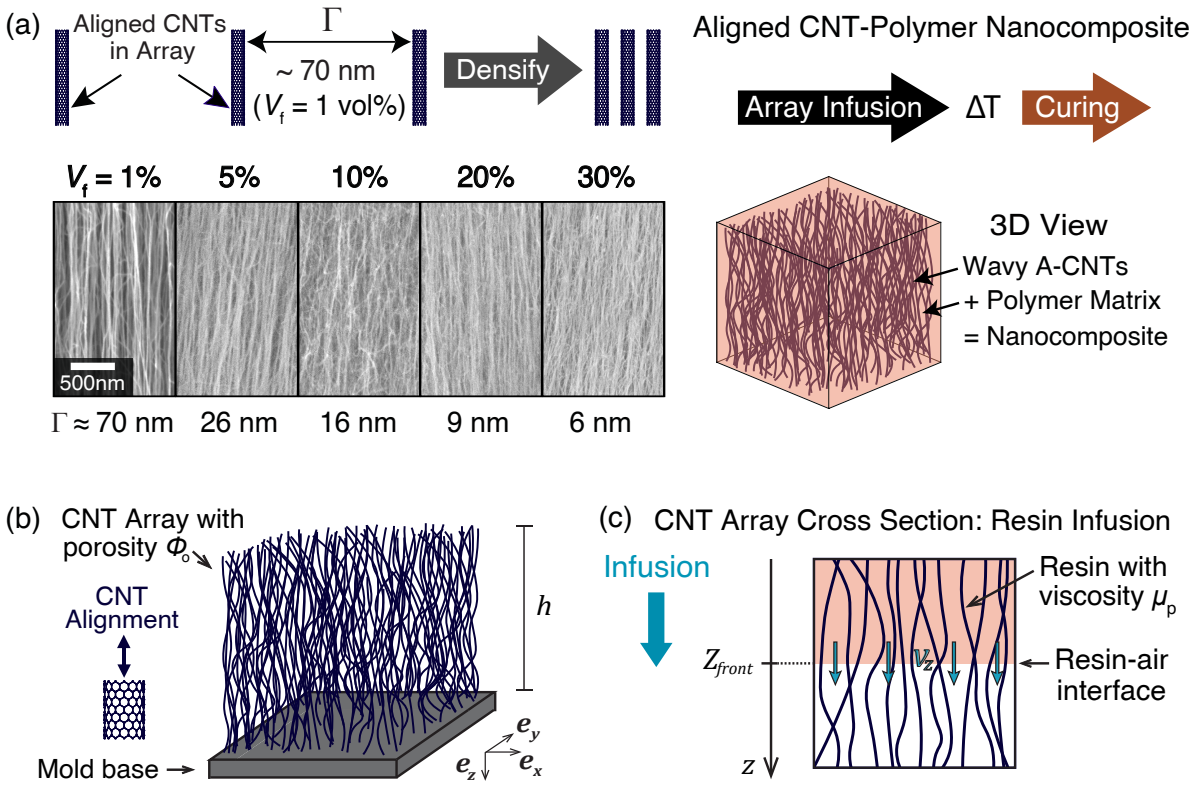


Figure 1: Overview of vertically aligned CNT array densification from 1 to 30 vol% for composite reinforcement, and the polymer infusion modeling framework for resin infusion. (a) Aligned CNT biaxial densification by mechanical compression increases CNT volume fraction ($V_f$) from 1 vol% (as-grown arrays) to 30 vol%, corresponding to decreased inter-CNT spacing ($\Gamma$) from ~70 to 6 nm with maintained vertical CNT alignment, as shown by exemplary SEM images of densified wavy A-CNT arrays at each CNT $V_f$. Illustration of a fully infused and cured aligned CNT-polymer nanocomposite. (b) Schematic describing the aligned CNT array geometry and the relevant directions and coordinate systems for the 1D vertically aligned CNT array model. (c) Schematic of resin infusion into aligned CNT arrays along the CNT alignment direction, where complete resin infusion is achieved for $Z_{\text{front}}(t = t_{\text{inf}}) = z/h = 1$ at infusion time $t_{\text{inf}}$.

recent molecular dynamics simulations have predicted a ~1 nm-thick interphase layer for epoxies surrounding CNTs,[24] as corroborated by experiments,[26] highlighting the utility of both computational and experimental studies to inform composite design *via* interfacial engineering.[18] It is possible and even likely that the entire polymer matrix can be affected by CNT confinement if only a few nanometers of space exist for the polymer chains to reside between each CNT in a high CNT $V_f$ PNC.[7] While recent work highlights the importance of understanding these confinement and interphase effects in nanoparticle-reinforced polymer

composites broadly,[25] there is still a lack of understanding of how these interactions vary across inter-CNT spacings and a range of polymers, such as high-performance aerospace-grade thermoset and thermoplastic resins commonly used in prepreg forms.

To address these challenges and investigate the potential use of uniform high-density ($\geq$ 20 vol% CNT $V_f$) architectures for next-generation composite reinforcement, this work describes an experimental and modeling process-structure-property study of mechanically-densified A-CNT PNCs to probe nanoscale interactions and inter-CNT spacings at the $<$ 10 nm scale using two aerospace-grade thermoset polymer matrices: CYCOM 977-3 epoxy resin and CYCOM 5250-4 bismaleimide (BMI) resin, which are chosen for their use in current prepreg systems. This study focuses primarily on 5250-4 BMI due to its use as a high-$T_g$ structural thermoset prepreg polymer, known for its higher load transfer capabilities compared to epoxy as well as high toughness, service temperature, thermal and chemical resistance, tensile strength, low viscosity, and because it is shown to be advantaged as a matrix for CNTs by recent computational molecular modeling results.[19,27] 977-3 epoxy PNCs are therefore considered as a standard for reference. The process-structure-property relationships of these PNCs are studied as a function of CNT $V_f$ to show how polymer confinement in densely packed A-CNT arrays up to 30 vol% CNT $V_f$ influences PNC fabrication and polymer infusion modeling, wetting, PNC structural evolution, CNT-matrix morphology, CNT alignment, thermal stability and curing, and mechanical properties *via* nanoindentation testing and modeling. Through these analyses, this work contributes new insights supporting the design of high CNT $V_f$ architectures for the development and integration of nano-engineered hybrid materials.

# Results and Discussion

## Polymer Infusion Modeling and Experimental Results for Aligned-CNT PNC Fabrication

Resin infusion modeling to establish the successful fabrication process of nanocomposites is presented, followed by detailed thermal and structure characterization of the resulting textured PNCs, and their mechanical properties, all as a function of textured A-CNT vol%. Lastly, a process to scale the textured high vol% PNCs in film and laminate form is presented. A-CNT arrays synthesized by chemical vapor deposition (see Methods) were densified *via* biaxial mechanical densification[7,28] as seen in Figure 1a, which shows an illustration of densification and a series of SEM images showing the vertically aligned CNT array morphology for each CNT $V_f$ as the inter-CNT spacing ($\Gamma$) decreases. Here, the CNT $V_f$ ranges from 1 vol% to 30 vol% with inter-CNT spacings of ~70 to 6 nm.[22,29] Since the polymer infusion limits into these arrays may be affected by the decreasing porosity within the higher CNT $V_f$ A-CNT packings,[30] a polymer infusion model is created and applied to the PNCs to support process development towards achieving full BMI and epoxy resin infusion into densely packed A-CNT arrays.

To describe the infusion of uncured polymer resin, a 1D A-CNT network model based on Darcy's Law and capillary-driven flow is developed. This framework models the through thickness infusion of the aerospace thermosets into a vertically aligned CNT array along the CNT axis direction ($e_z$). Figure 1 shows model schematics illustrating how resin infuses along the CNT alignment direction, *i.e.* into CNT arrays of height $h$. Both the A-CNT array and resin infusion are non-isotropic due to the CNT alignment, and Darcy's law is used to provide an analytical expression of the displacement of the liquid-air interface moving into the array along the $e_z$ direction with time due to a capillary pressure drop, similar to prior work on 1D polymer resin flow into aligned fiber networks.[31,32]

The capillary pressure, $p$, as shown in Eq. 1,[31,33] is the driving force for polymer infu-

sion that increases with increasing CNT $V_f$ (porosity decrease), and this is opposed by the decreasing permeability of the A-CNT array with CNT $V_f$, $K_{array}$, as shown in Eq. 2 for the flow parallel to a randomly non-overlapping unidirectional fibrous structure.[33–35] Here, $\phi_o$ is the porosity of the CNT array as a fraction of 1 (*i.e.* 1− CNT $V_f$, so a 1 vol% A-CNT array has a porosity $\phi_o$ of 99%), $r_{cnt}$ is the outer radius of an individual CNT, $\gamma_{cnt}$ is the surface energy of the CNTs, and $\gamma_{p,cnt}$ is the interfacial energy between the CNT and polymer. Due to the A-CNT array porosity decrease from 0.99 to 0.7 from 1 vol% to 30 vol% A-CNTs, $p$ increases by ∼40× from 1 vol% to 30 vol% A-CNTs, and the permeability of the A-CNT array decreases by ∼2500×, which yields long polymer infusion times at high volume fractions (see Section S1 of the Supporting Information for derivation and further discussion).

$$p = \frac{2(\gamma_{cnt} - \gamma_{p,cnt})(1 - \phi_o)}{\phi_o r_{cnt}} \tag{1}$$

$$K_{array} = \frac{r_{cnt}^2 \phi_o^3}{8(1 - \phi_o)^2} \tag{2}$$

Incorporation of these factors into Darcy's law mathematically relates the position of the resin front to the elapsed infusion time $t$ following the expression:

$$t = \frac{Z_{front}^2(t)}{2} \frac{8\mu_p h^2 (1 - \phi_o)}{2(\gamma_{cnt} - \gamma_{p,cnt}) r_{cnt} \phi_o^2} \tag{3}$$

where $t$ is the time, $Z_{front}$ represents $z_{front}$ normalized by the array height $h$, giving the position of the liquid-air interface along the CNT alignment direction as a function of time $t$, and $\mu_p$ is the dynamic viscosity of the neat uncured polymer. When the array is fully infused with resin, $Z_{front}(t)$=$z_{front}(t)/h$=1, and the time of infusion is:

$$t_{inf} = \frac{2(1 - \phi_o)\mu_p h^2}{(\gamma_{cnt} - \gamma_{p,cnt}) r_{cnt} \phi_o^2} \tag{4}$$

which is the full infusion time ($t_{inf}$) of the resin into an A-CNT array of height $h$. Additional

modeling details and derivation can be found in Section S1 in the Supporting Information. In this way, the time required for full resin infusion into the A-CNT array depends on the capillary pressure, permeability, the geometry of the CNT network through $r_{cnt}$, $\phi_o$, and $h$, as well as the physical properties of the resin and CNTs *via* the interfacial energy difference $\gamma_{cnt}-\gamma_{p,cnt}$, and the polymer resin viscosity $\mu_p$. At high CNT $V_f$, the significantly decreased permeability overcomes the increased capillary pressure driving force, yielding drastically longer infusion times. Therefore, this framework shows that to yield shorter infusion times at high CNT $V_f$, the viscosity of the resin may be decreased to speed up infusion and achieve fully infused A-CNT PNCs.

This polymer infusion model is then applied to inform the successful fabrication of A-CNT PNCs (*i.e.* provide insight into achieving full resin infusion at increasing CNT $V_f$). The fabrication of A-CNT PNCs using the two aerospace-grade resins (see Methods) is presented in Figure 2, which shows an illustration of the vacuum-assisted and capillary-driven infusion of resin into A-CNT arrays within a steel mold (Figure 2a), optical micrographs of densified A-CNTs and A-CNT PNC fabrication (Figure 2b), and the final CNT PNCs along with cured neat resin baselines (Figure 2c). Neat resins were heated to 120°C for infusion under vacuum of 1 vol% and 5 vol% low-CNT $V_f$ PNCs with each type of polymer matrix, as previously demonstrated for 20 vol% CNT $V_f$ PNCs using different epoxy resins.[7,12] For higher-CNT $V_f$ PNCs, diluted 65 wt% resin-acetone solutions with lower viscosity were used instead (discussed next with the application of the polymer infusion model), and these solutions were poured into the 10−30 vol% molds at room temperature (25°C) for capillary-assisted infusion into the high $V_f$ CNTs. Acetone was used due to its low viscosity (useful for thinning), low boiling point (easy to dry before curing), and since it is a good solvent for both resins.[36] After infusion, the PNCS were dried in a vacuum oven to fully remove the acetone[36] prior to curing following the manufacturer's cure cycle. SEM cross-section analysis discussed next showed that CNT alignment due to 'bumping' from solvent removal was not observed, and any irregularities in the top PNC surface may be attributed to the micron-scale entangled

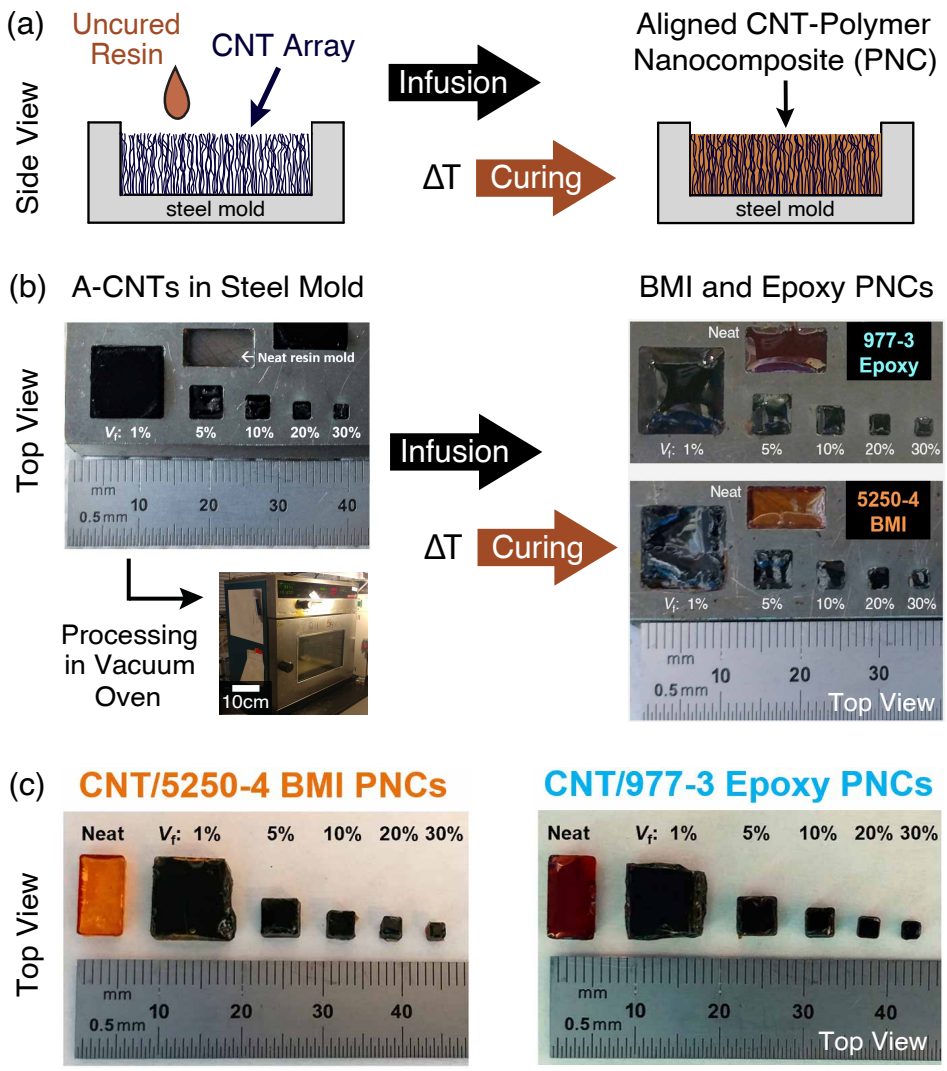


Figure 2: Overview of the fabrication of aligned CNT-polymer matrix nanocomposites (PNCs), where 1−30 vol% A-CNT arrays are infused with aerospace-grade 977-3 epoxy and 5250-4 BMI resin matrices. (a) Side-view schematics of neat uncured resin infusion and curing in a steel mold. (b) Top-down view optical micrographs of A-CNT arrays before and after resin infusion and curing in a vacuum oven following the manufacturer's cure cycle, where the resin is infused *via* the vacuum-assisted capillary-driven wetting of A-CNT arrays. (c) Top-down view optical micrographs of the final cured A-CNT PNCs at each CNT $V_f$, including a cured neat resin baseline.

CNT layer on top of the array from CNT synthesis. Additional details can be found in Section S2 in the Supporting Information.

The model-predicted infusion times for neat BMI and epoxy resin infusion at 120°C and dilute BMI-acetone and epoxy-acetone solution infusion at 25°C as a function of CNT $V_f$ (for

1−30 vol% A-CNTs) using Eq. 4 are shown in Figure 3a. As CNT $V_f$ increases, the porosity of the A-CNT array decreases, and longer infusion times are required. Neat resin infusion into 1 vol% and 5 vol% A-CNT arrays can be completed during 2 h of infusion, the approximate

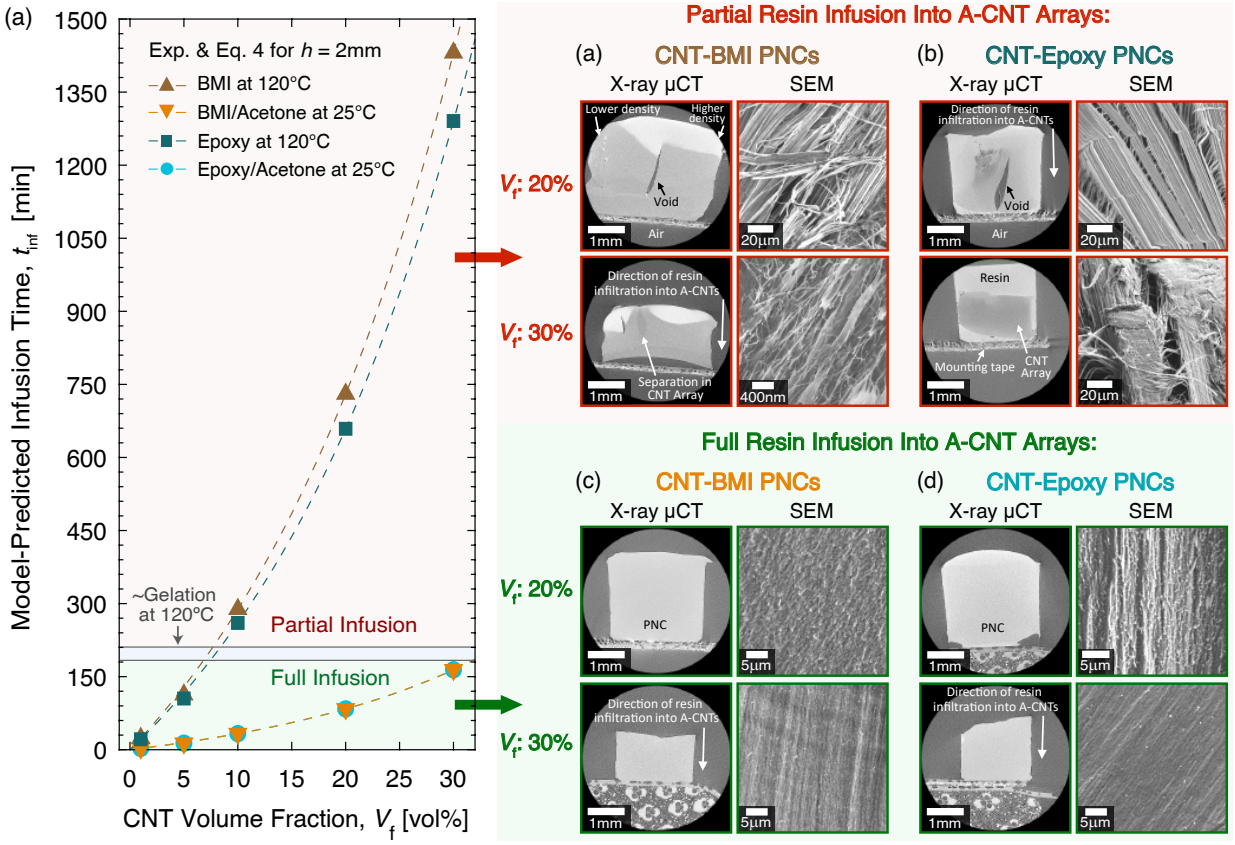


Figure 3: Textured A-CNT PNCs by resin infusion experiments and modeling as a function of CNT volume fraction leading to neat BMI and epoxy resin infusion at the recommended handling temperature of 120°C, as well as for diluted 65 wt% BMI- and epoxy-acetone solution infusion into A-CNT arrays at 25°C. (a) Model-predicted infusion time (dashed lines) versus CNT $V_f$ for a 2mm-tall A-CNT array, and experimental data (markers). Regions of experimentally observed (b) incomplete/partial infusion (red, top region, neat resin, $\mu_p$∼3000 cP) and (c-d) full infusion (green, bottom region, diluted resin, $\mu_p$∼350 cP) are included. Representative X-ray μCT images at 2μm voxel size and SEM images of mechanical hand-fracture surfaces for the 20 vol% and 30 vol% CNT $V_f$ PNCs show that incomplete infusion results in non-homogeneous composite morphology, as seen by the presence of non-wetted CNTs, separated CNT array sections, microvoids, and both lighter and darker color intensities in the X-ray μCT images, which correspond to high- and low-density areas, respectively. Full resin infusion at the micron-scale is achieved when diluted resin is used during processing, which results in a homogeneous composite morphology without microvoids (dark regions), CNT array separation/aggregation, or variations in density.

limit before viscosity increases towards gelation occurring $\gtrsim$3 h into processing. To achieve full infusion, higher CNT $V_f$ arrays (10−30 vol%) that require $>$ 3 h of infusion time at the elevated processing temperature with neat resin should instead be infused with the ∼10 × lower viscosity resin solutions at 25°C (see Section S2 in the Supporting Information for viscosity measurements), which enables shorter infusion times due to the lower viscosity compared to the neat resin, following Eq. 4. Solution infusion here also occurs at room temperature (25°C), so thermally-induced gelation through cross-linking and polymer chain growth are not a factor.

To determine if the infusion time is adequate for composite fabrication after curing is complete, the PNCs were imaged by a Zeiss Xradia 520 Versa X-ray micro-computed tomography (μCT) tool at a 2 μm voxel size to analyze cross sections of the internal structure (see Figure 3b-c). X-ray μCT is a non-destructive technique that is employed here to provide two-dimensional (2D) cross-section images and three-dimensional (3D) bulk volume renderings of the PNC interior to visualize the extent of polymer infusion at the micro-scale, including partial infusion noted by micro-scale voids or lower-density areas.[37] It is used to identify the presence of microvoids resulting from different process conditions, along with variations in density (where bright color signifies high density and dark color signifies low density), which would indicate incomplete infusion as shown in Figure 3b. In addition, nanoindentation testing can reveal if the infusion time is insufficient, as the indentation moduli of only partially infused composites was found to be significantly lower (MPa range) than the fully infused composite values (GPa range) discussed later in this report, and these moduli were similar to the indentation moduli of neat A-CNT arrays measured in prior work.[11] The PNCs were also hand-fractured (cross-sectioned) with a razor blade at room temperature to study their morphology *via* SEM to check for poor resin-CNT wetting, voids, and CNT aggregation, which would also indicate incomplete infusion. In contrast, full infusion, as shown in Figure 3c, is noted by a consistent and even bulk structure, density, and internal morphology.

Figure 3 shows the X-ray μCT and SEM results of infusion with both neat and diluted resins into the highest $V_f$ A-CNT arrays (20 and 30 vol%), demonstrating that full infusion is achieved when diluted resin is used (denoted in green), and incomplete infusion occurs when neat resin is used (denoted in red), which is consistent with the model results in Figure 3a. Incomplete infusion results in non-homogeneous composite morphology, as seen by the presence of non-wetted CNTs, separated CNT array sections, microvoids, and both lighter and darker color intensities in the X-ray μCT images, which correspond to high- and low-density areas, respectively. Full resin infusion at the micron-scale is achieved when diluted resin is used during processing, which results in a homogeneous composite morphology without microvoids, CNT array separation/aggregation, or variations in density. Therefore, neat resin can be used for the fabrication of low CNT $V_f$ BMI and epoxy PNCs, whereas diluted resin is preferable for the infusion of high CNT $V_f$ BMI and epoxy PNCs to enable the process-structure-property relations of fully infused PNCs as a function of CNT $V_f$.

Following these synthesis results, the μCT images in Figure 4 confirm full resin infusion at the micron scale into the 1−30 vol% CNT $V_f$ A-CNT arrays for the BMI PNCs (see Figure S5 for epoxy PNCs), as shown by the even gray color within each PNC denoting uniform density and no microvoids, consistent with cured neat resin samples. In addition, the SEM micrographs of the PNCs can be studied to probe CNT confinement effects influencing polymer infusion, CNT-matrix morphology, CNT-polymer wetting, dispersion, and particularly the CNT alignment within the polymer matrix and PNC microstructure after infusion and curing. SEM analysis also shows the fracture surface cross sections detailing the fracture behavior for BMI and epoxy, including CNT pull-out from the matrix and bridging, indicating the relative CNT-matrix interaction strength based on CNT $V_f$.[25] The SEM micrographs show that the polymer matrices fill the spaces between the A-CNTs for each CNT $V_f$, with wetting achieved for up to 30 vol% PNCs, as well as maintained CNT alignment and dispersion in the matrix upon resin infusion and curing. This is consistent with the full infusion of ∼20 vol% CNT $V_f$ A-CNTs from prior work that fabricated A-CNT PNCs using

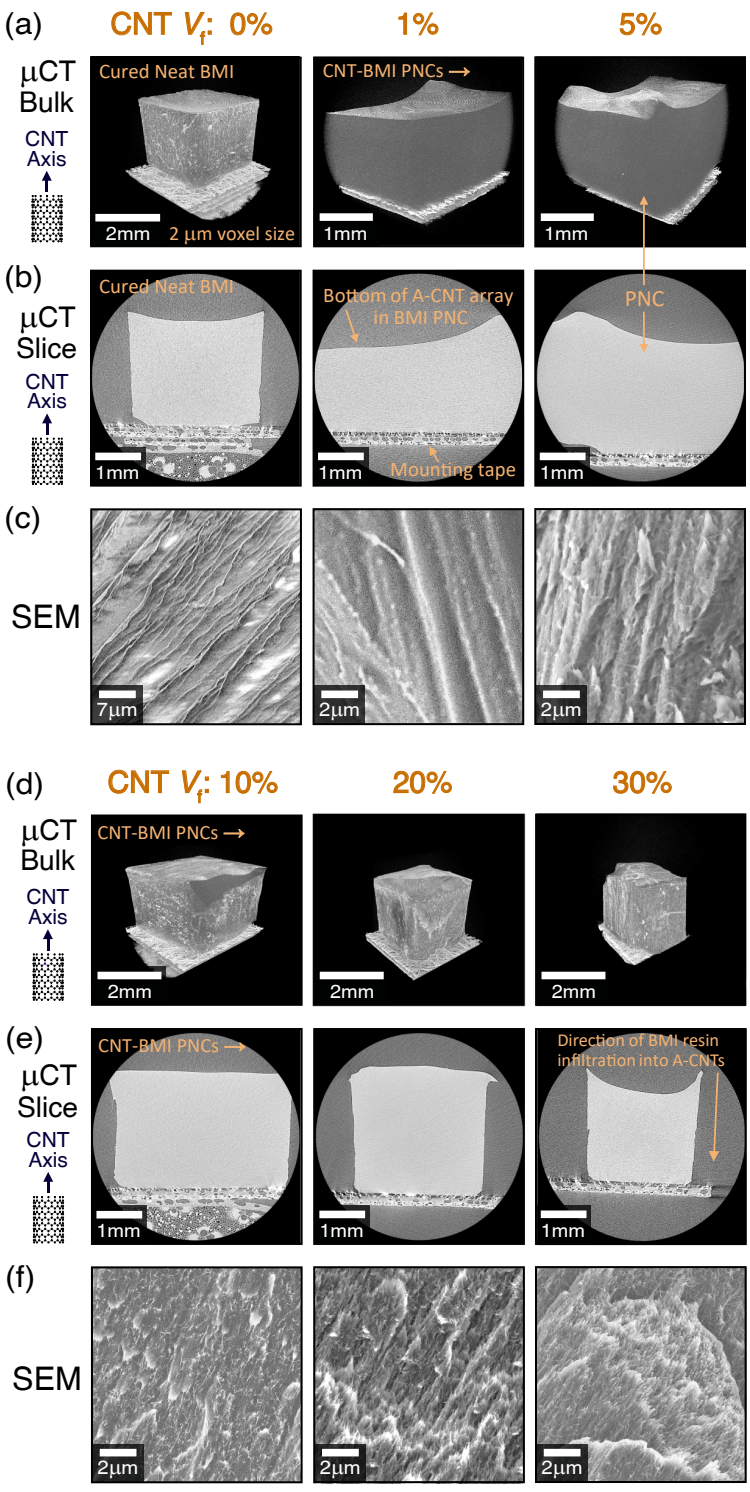


Figure 4: Visualization of fully infused and cured CNT-BMI PNCs *via* 3D X-ray μCT images, cross-sectional (2 μm voxel size) 2D X-ray μCT slices, and SEM images of hand-fracture surfaces with CNT $V_f$ for: (a-c) low CNT $V_f$ (0-5 vol%), and (d-f) high CNT $V_f$ (10-30 vol%) PNCs, showing a uniform density, thorough CNT-BMI wetting, consistent CNT alignment and dispersion, and CNT pullout from the matrix as a result of fracture for each CNT $V_f$.

different epoxies[7,12] and demonstrates the feasibility of processing these resins into higher CNT $V_f$ A-CNT arrays using dilution techniques. Additional morphological characterization supporting these results can be found in Section S3 of the Supporting Information, including higher resolution X-ray μCT and comparisons between neat A-CNTs, polymer, and PNCs, micron-scale SEM fracture surfaces for both PNCs, and cross-sectional TEM imaging of a 30 vol% CNT BMI PNC showing full polymer infusion and CNT alignment at the nano-scale (Figure S7). This analysis gives a qualitative indication of the relative strength of CNT-matrix interactions and pull-out behavior as a function of CNT $V_f$ in the PNCs, as corroborated by structural, thermal, and mechanical testing discussed next that provide additional insight into CNT reinforcement effects and bulk PNC properties.

## Thermal Stability and Curing as a Function of CNT Volume Fraction

Analysis of the thermal behavior of A-CNT/BMI and A-CNT/epoxy PNCs in nitrogen is performed to assess the thermal stability and curing with increased A-CNT loading, providing information about the polymer degradation stages, charring, relative CNT and polymer mobility in composites, cross-linking, and curing as CNT $V_f$ increases. Since the CNTs do not show significant thermal degradation in nitrogen, these thermal tests are performed to separate out polymer confinement effects. Differential scanning calorimetry (DSC) giving degree of cure (DoC) and $T_g$ evolution as a function of CNT $V_f$ is shown in Figure 5, and thermogravimetric analysis (TGA) giving CNT weight% and decomposition onset temperature evolution as a function of CNT $V_f$ is shown in Figure 6. Representative DSC curves from the first heating cycle of BMI PNCs (Figure 5a) show complete BMI curing during composite fabrication, as seen by a ~95% DoC for the neat resin and all tested CNT $V_f$ PNCs,[28] where the lack of a large exothermic peak is observed for the neat resin and cured PNCs compared to the large exothermic peak observed for the uncured neat resin at 250°C. This is consistent with prior observations for low vol% CNT-BMI composites[38] and carbon

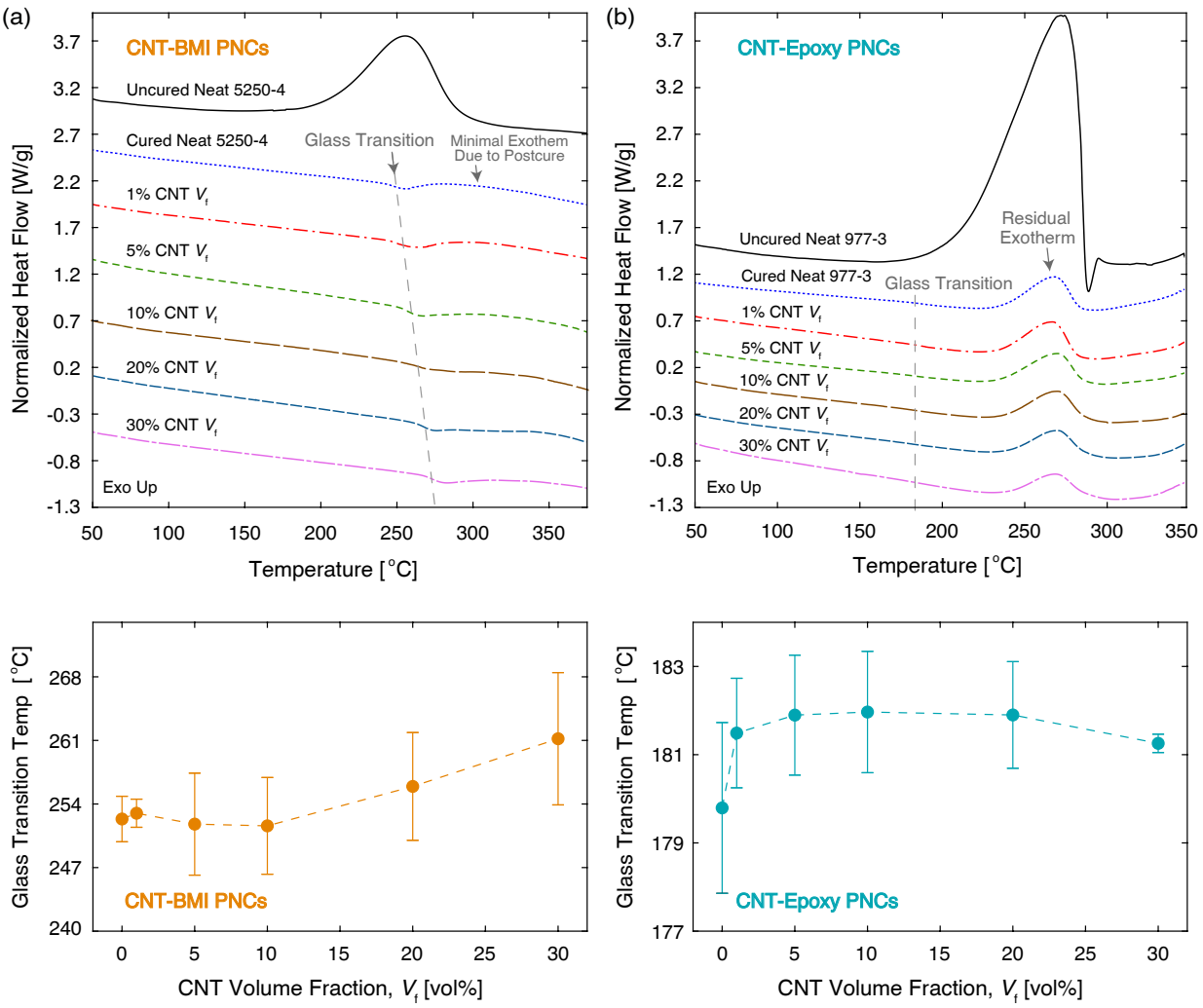


Figure 5: Thermal behavior of uncured neat BMI and epoxy resin and cured CNT-BMI and CNT-epoxy PNCs as a function of CNT $V_f$, as measured by differential scanning calorimetry (DSC) experiments in nitrogen. (a) Representative DSC curves from the first heating cycle show complete BMI curing during CNT-BMI PNC fabrication, and plot showing that a consistent glass transition temperature is observed for the cured neat resin and all tested PNCs with 1−30 vol% aligned CNTs in the BMI matrix. (b) Representative DSC curves from the first heating cycle show full epoxy curing during CNT-epoxy PNC fabrication, and plot showing that a consistent glass transition temperature is observed for the cured neat resin and all tested PNCs with 1−30 vol% aligned CNTs in the epoxy matrix.

fiber/BMI composites.[39] A maintained $T_g$ in the manufacturer's range of ∼215−290°C is also observed for the cured neat resin and all tested PNCs with 1−30 vol% aligned CNTs in the BMI matrix, as noted by the endothermic transition in this region (here ∼260°C), consistent with literature for neat resin and low vol% CNT PNCs.[36,40] This range is large

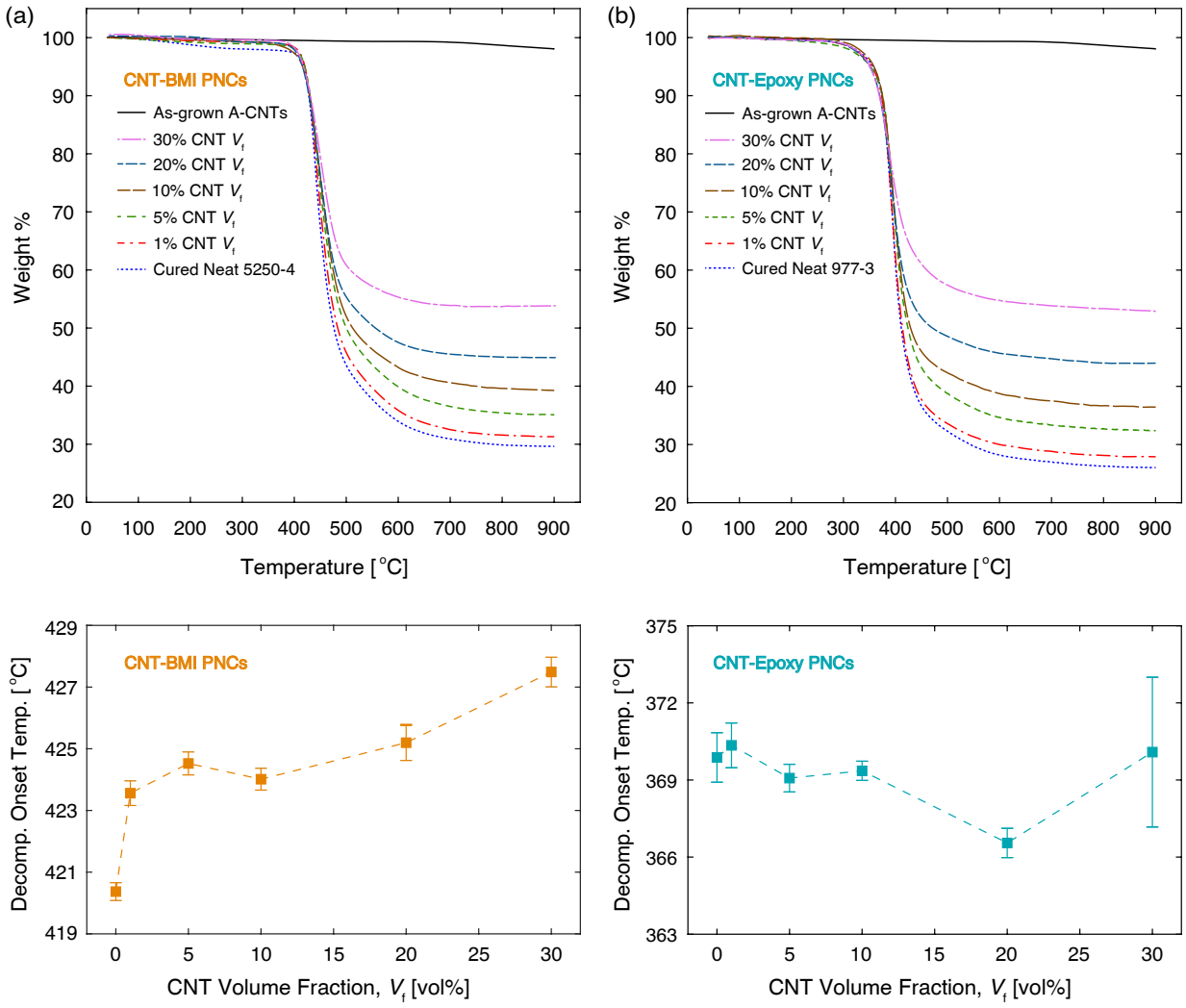


Figure 6: Thermal behavior of cured neat BMI and epoxy resin, aligned CNTs, and CNT-BMI and CNT-epoxy PNCs as a function of CNT $V_f$, as measured by thermogravimetric analysis (TGA) experiments in nitrogen. (a) Representative TGA curves confirm the full curing of the BMI resin at each CNT $V_f$, an expected CNT weight percent increase with CNT $V_f$ in the PNCs, and plot showing that the decomposition onset temperature of the BMI resin increases with CNT $V_f$, indicating higher thermal stability of the PNCs. (b) Representative TGA curves confirm the full curing of the epoxy resin, an expected CNT weight percent increase with CNT $V_f$ in the PNCs, and plot showing that the decomposition onset temperature of the epoxy resin is approximately constant with increasing CNT $V_f$, indicating maintained thermal stability.

due to several different postcuring cycles tested by the manufacturer for the neat BMI resin that are reported. Representative DSC curves from the first heating cycle of epoxy PNCs (Figure 5b) also show full epoxy curing during composite fabrication, as seen by a ~92%

DoC for the neat resin and all tested CNT $V_f$ PNCs,[28] similar to literature for low vol% CNT-epoxy composites.[41] A consistent $T_g$ in the manufacturer's range of ~178−190°C is observed, signifying that the confinement of polymer at these length scales does not largely affect this thermal transition in the PNCs. A larger endothermic transition representing the $T_g$ is observed for BMI compared to epoxy, which may be attributed to the additional thermal history/physical aging (*via* the postcuring process) of the BMI, which has previously been observed to increase the magnitude of enthalpic relaxation/recovery endotherm during DSC testing.[42]

Representative TGA curves in Figure 6a also confirm the full curing of the BMI resin due to the consistent degradation rates with CNT $V_f$ that are observed after 400°C, and where slightly delayed thermal decomposition behavior (increased thermal stability) is observed as CNT $V_f$ increases, which may be attributed to the favorable interaction of the aromatic backbone of the BMI polymer chain with the CNT walls.[43] Here, the decomposition onset temperature of the BMI resin increases by ~8°C with CNT $V_f$ (~420°C in BMI to ~428°C in 30 vol% BMI PNCs), indicating higher thermal stability of the PNCs with increased amounts of A-CNT reinforcement. The as-grown A-CNT arrays are observed to have a high thermal stability, as they only exhibit a weight loss of ~3 wt% as the temperature increases to 900°C in nitrogen. This indicates that only a small amount of amorphous carbon is present on the outer CNT walls from the CNT synthesis procedure, as this amorphous carbon is observed to degrade at $\gtrsim$300−400°C.[44] For both BMI and epoxy PNCs, the CNT wt% increases beyond 20 vol% as expected in the PNCs and scales with the CNT $V_f$ established by the array geometry during PNC fabrication. Representative TGA curves in Figure 6b also confirm the full curing of the epoxy resin due to the consistent degradation rates observed after 360°C, and this thermal decomposition behavior is observed consistently as CNT $V_f$ increases (*i.e.* similar thermal stability across all tested CNT $V_f$). Here, the decomposition onset temperature of the epoxy resin is approximately constant at ~370°C with increasing CNT $V_f$, indicating the maintained thermal stability of the PNCs and minimal effects on the

polymer stability at decreasing inter-CNT spacings.

These results, which are the first reported for these two aerospace-grade resins reinforced by A-CNT arrays ranging from 1 to 30 vol%, provide high vol% thermal data in comparison to prior work showing that for thermosetting high-$T_g$ epoxy, BMI, and polyimide resins, there is often not a clear consensus on how CNT loading governs $T_g$, as these values can both increase and decrease compared to the neat resin as the CNT loading is varied.[28] This may be due to the high thermal conductivity of the CNTs compared to the matrix, low polymer chain mobility within the crosslinked network (compared to higher chain mobility in thermoplastics), and favorable or unfavorable CNT-matrix interactions that either inhibit or augment polymer chain mobility and relaxation dynamics, respectively.[45] Here, the $T_g$ is observed to increase with CNT $V_f$ up to 30 vol% for CNT-BMI PNCs (an initial increase for 1 vol% A-CNTs over the neat polymer, and then an increase after 10 vol% A-CNTs), whereas the $T_g$ is consistent across all tested CNT $V_f$ for CNT-epoxy PNCs. This corroborates past work using different BMI and epoxy resins that showed that ∼2−4 vol% CNT-BMI composites exhibited a ∼6% increase in $T_g$ over the neat resin[38,46] or no change at all,[36] ∼2 vol% CNT-epoxy composites could exhibit a ∼4% increase or 4% decrease in $T_g$,[41,47,48] and that there is often no change in $T_g$ for low-medium vol% CNT-epoxy composites. This was observed for 5 vol% randomly oriented carbon nanofiber reinforcement[49] and 8 vol% CNT reinforcement[50] in a tetraglycidyl epoxy matrix similar to the epoxy used here, indicating that the crosslinking density and thermal stability are not affected by CNT incorporation at the tested volume fractions. These results are in contrast to CNT-thermoplastic polymer composites at low vol%[45] that can often yield increases in $T_g$ due to ordering and interfacial interactions, as well as high vol%, such as CNT-poly(urethane-urea) elastomeric nanocomposites that exhibited ordered hard segment nanophases due to confinement at CNT $V_f$ of 10−30 vol%.[51,52] This study thereby demonstrates the maintained thermal stability of PNCs at high A-CNT vol% due to the thermosetting polymer matrix, particularly for unaltered aerospace-grade BMI and epoxy resins commonly used in prepreg forms, where future CNT

reinforcement without matrix degradation would be desirable for both structural and multifunctional property enhancements.[53]

## PNC Structure and CNT Alignment as a Function of CNT Volume Fraction

To investigate how the structure of high-density A-CNT-reinforced epoxy and BMI PNCs evolves with CNT $V_f$ in highly loaded CNT systems, and therefore provide new insight in comparison to much prior work on low vol% CNT-polymer systems,[54] X-ray diffraction (XRD) analysis is conducted to study the effects of polymer infusion, polymer type, and local confinement in the PNCs, here as a function of A-CNT orientation. In the representative diffraction patterns shown in Figure 7a (BMI) and 7b (epoxy), the (002), (100), and (110) carbon peaks are evaluated at positions of $2\theta \approx 26°$, 43°, and 78°, respectively,[54] which arise from the (100) and (110) carbon planes, and the broad epoxy and BMI peaks typical for thermosetting resins are observed at $2\theta \approx 18°$,[39,55] signifying the packing and crosslinking of polymer chains.[39] Because thermoset polymers such as the 977-3 epoxy and the 5250-4 BMI used here exhibit a cross-linked network structure after curing, they show a characteristic broad XRD peak below 26° owing to their amorphous structure as a result of the curing reaction.[7,39,55] The shape and evolution of the diffraction patterns are therefore observed to be similar for both epoxy and BMI matrix PNCs, and in the presence of A-CNTs, which has not previously been explored for 30 vol% CNT-BMI and CNT-epoxy composites with a high degree of CNT alignment. Finally, this polymer peak is similar in both the orthogonal and parallel XRD orientations, as its amorphous structure is consistently observed at each CNT $V_f$. This suggests that there is not a preferential ordering or orientation of the polymer chains due to increased confinement between CNTs in either the horizontal or vertical CNT alignment direction, even at high CNT vol% where the inter-CNT spacing (∼5 nm) is similar to the radius of gyration of the polymers, also on the order of ∼5 nm, as expected considering the cross-linked nature of the studied resins.

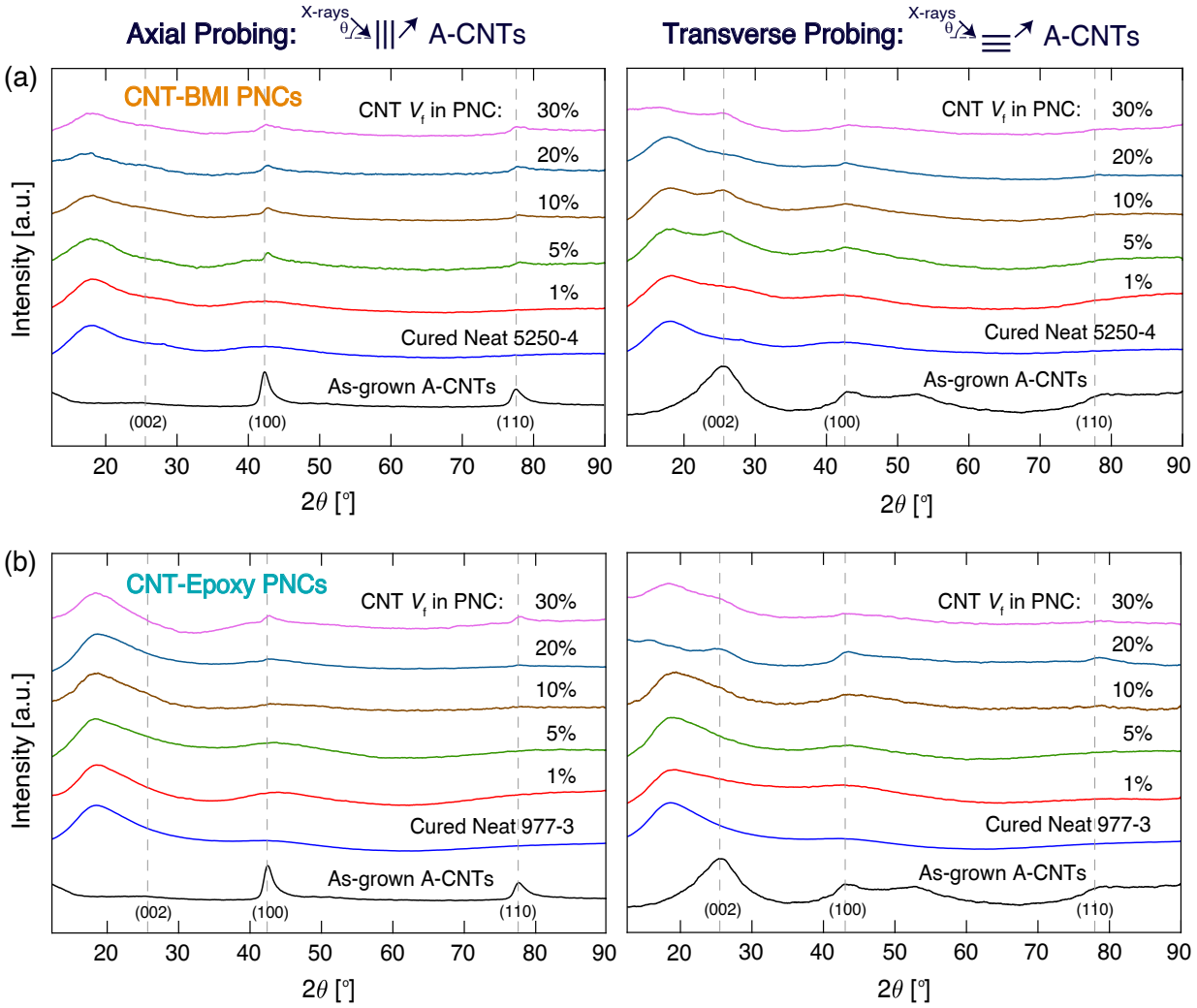


Figure 7: Probing textural differences in aligned-CNT PNCs *via* X-ray diffraction (XRD) diffraction patterns, (a) neat cured BMI and CNT-BMI PNCs, and (b) neat cured epoxy and CNT-epoxy PNCs with 1−30 vol% CNT $V_f$ CNTs, where CNT alignment is orthogonal and parallel to the XRD stage as illustrated above the plots. The diffraction patterns show maintained CNT alignment and the evolution of the (002), (100), and (110) carbon peaks at $2\theta \approx 26°$, 43°, and 78°, respectively, and the broad amorphous BMI and epoxy peak at $2\theta \approx 18°$. The (002) peak of the CNTs is only observed in the parallel CNT alignment configuration, as only this sample geometry allows diffraction from the CNT walls since they are parallel to the XRD stage.

Due to the A-CNT vertical alignment in the as-grown array and the epoxy and BMI PNCs, the (002) carbon peak due to the inter-layer spacing of the CNT walls at $2\theta \approx 26°$ is not probed when the A-CNTs are oriented orthogonal to the XRD stage, as no diffraction from the CNT walls is possible in this geometry if the CNTs are vertically aligned. Although

CNT waviness might cause some contribution, none is observed here. Therefore, this peak is not seen in the axial orientation diffraction patterns, signifying that the CNTs maintain their vertical alignment after the densification, polymer infusion, and PNC curing steps. These results corroborate the CNT alignment observed in the SEM micrographs and are consistent with past work demonstrating near-zero (002) peak intensity for A-CNTs characterized in this X-ray geometry.[56] In contrast, the (002) peak is clearly visible in the transverse orientation, where the primary CNT axis is parallel to the XRD stage. In this geometry, X-ray diffraction can occur from the CNT walls in all PNCs, and the (002) peak is clearly observed as a shoulder that broadens the ∼18° polymer peak compared to the orthogonal A-CNT PNC orientation, where this shoulder is not visible.

Through this analysis of the high vol%, nanometer-scale confinement regime in A-CNT PNCs, the A-CNTs are observed to contribute more to the diffraction patterns at higher CNT $V_f$ for both types of PNCs, and the patterns are observed to be superpositions of CNT and epoxy/BMI features since no new peaks are present for CNT $V_f$ up to 30 vol%. This is consistent with the Raman spectroscopy results discussed in Section S4 in the Supporting Information. If a new peak is observed, it could suggest the presence of a structurally distinct polymer interphase approximately 1−100 nm in the vicinity of the CNTs,[12,21] particularly for thermoplastics with high polymer chain mobility, which is plausible for the nm-scale inter-CNT spacings achieved here. However, since no additional peaks alongside those previously described are observed up to 30 vol% CNT $V_f$, this suggests that the epoxy and BMI do not form a measurably distinct polymer interphase region in these PNCs. This can be expected due to the low polymer chain mobility in the crosslinked network of the thermoset resins studied here, consistent with past work on bulk CNT-epoxy PNCs.[7,12] The ∼18° polymer peak of the amorphous thermoset matrix is consistent across all CNT $V_f$ and in both orientations, indicating that the as-received polymer does not exhibit a preferential alignment within the composites. Finally, the consistent positions of the (100) carbon peak (∼43°) and the (110) carbon peak (∼78°) for all PNCs indicate that the confined CNTs

at high CNT $V_f$ do not significantly influence the polymer packing or curvature in these directions. The CNTs at higher CNT $V_f$ contribute more to the diffraction pattern owing to the superposition of CNT and polymer features, demonstrating that PNCs with a preserved polymer structure can be fabricated even at high loadings of A-CNTs, where additional property improvements can be obtained as discussed next.

## Scaling of Anisotropic Stiffness with CNT Volume Fraction

To understand how high A-CNT packing densities in BMI and epoxy matrices affect the mechanical properties of PNCs, microstructural mechanical characterization is performed *via* nanoindentation testing with a diamond Berkovich tip. In particular, the local quasi-static mechanical properties and degree of anisotropy between axial and transverse CNT orientations are quantified for previously unexplored high vol% A-CNT BMI and epoxy PNCs. This method has previously been applied to similar materials including neat A-CNT arrays,[11] and polymer composites including those incorporating BMI[57,58] and epoxy matrices[12,59,60] to evaluate the indentation modulus. However, an understanding of the mechanical indentation response at high A-CNT vol% in these high performance resins has not yet been determined, and is evaluated in this work.

Figure 8 shows the scaling of the axial and transverse (*i.e.* parallel/longitudinal and perpendicular) indentation modulus of the BMI and epoxy PNCs after fabrication, curing, and microtoming (see Methods). For both the BMI and epoxy PNCs, the transverse force-displacement curves (see Section S5 of the Supporting Information for additional details and data sets) exhibit a similar mechanical response at all CNT $V_f$ due to being polymer matrix-dominated in this orientation,[9,61] while the axial curves show a significantly enhanced mechanical response as CNT $V_f$ increases from 0 to 30 vol% (*i.e.* a smaller maximum indentation depth with a larger slope at the point of unloading) due to alignment with the CNT axial direction. As shown in Figure 8, this results in a $\sim$2 $\times$ increase in the axial indentation modulus and anisotropy ratio (axial/transverse) for 30 vol% CNTs compared

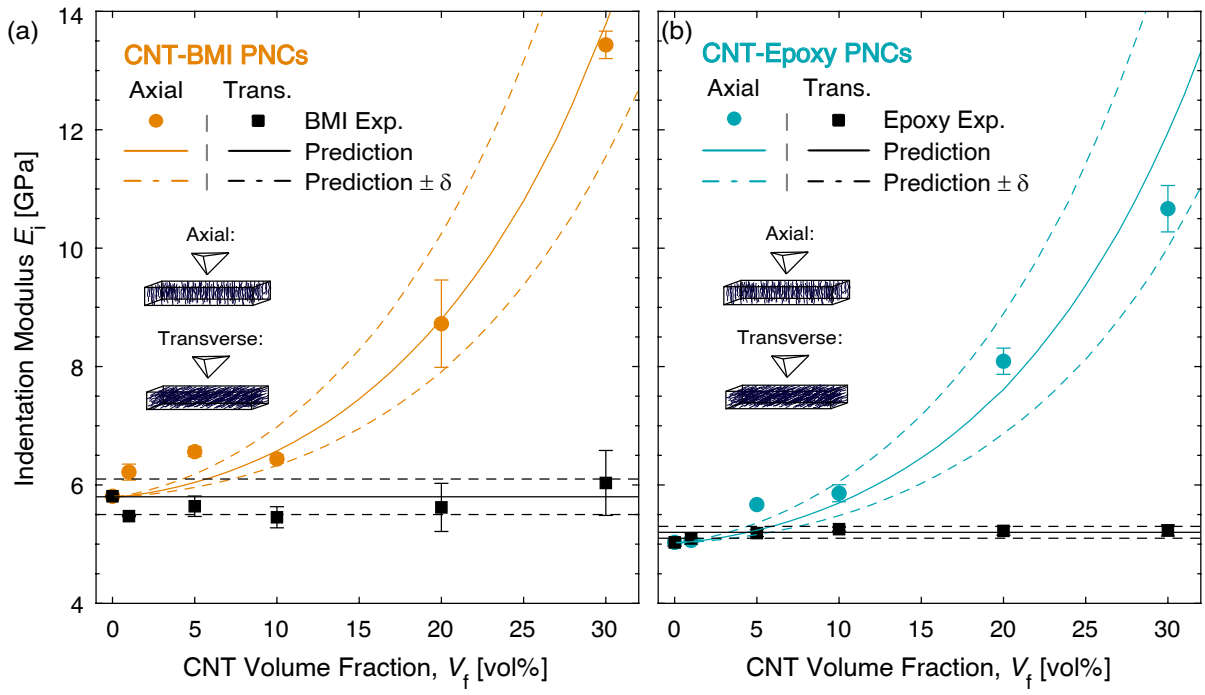


Figure 8: Scaling of the axial and transverse indentation modulus with CNT $V_f$ for: (a) CNT-BMI and (b) CNT-epoxy PNCs from quasi-static nanoindentation testing assuming an elastic response upon unloading. Plots show a ∼2 × increase in the axial indentation modulus and anisotropy ratio for the 30 vol% CNT PNCs as compared to neat resin, and they demonstrate a non-linear evolution with $V_f$ as described by Eq. 5 for simulated A-CNT PNCs comprised of $10^4$ CNTs. The transverse indentation modulus is approximately constant and unaffected by CNT $V_f$, since that mechanical response is expected to be matrix-dominated.

to the cured neat resin: ∼5.8 to 13.43 GPa in BMI PNCs with an anisotropy ratio up to 2.23 compared to ∼5.0 to 10.67 GPa in epoxy PNCs with an anisotropy ratio up to 2.04. The mechanism for this behavior is correlated to the columnar compression of A-CNTs along their long axis that provides standard long-fiber composite reinforcement as evidenced by enhanced stiffness in this orientation compared to transverse loading, and therefore the CNTs contribute more to the PNC mechanical response at high CNT $V_f$ in their axial orientation.[12,15,52,62]

Approximately constant transverse indentation moduli are observed across all $V_f$ (∼5.9 GPa for BMI PNCs and ∼5.2 GPa for epoxy PNCs), showing that CNT reinforcement effects are primarily dominant in the axial orientation and thereby increase the anisotropy ratio as $V_f$ increases. This result is consistent with prior work that found little enhancement

in the transverse modulus for 1−18 vol% aligned CNT-epoxy PNCs measured *via* uniaxial tensile testing.[15] For the cured neat 5250-4 BMI and 977-3 epoxy resins in this work, the modulus was 4.6 GPa for BMI (tensile modulus) and 3.8 GPa for epoxy (flexural modulus). The indentation moduli here for the cured neat resins and low vol% PNCs are slightly higher than these values (∼5.8 GPa for neat BMI and ∼5.03 GPa for neat epoxy) which is consistent with previous nanoindentation studies of neat BMI[57,58] and epoxy resins,[12,59,60] where indentation moduli in the ∼3-5 GPa range for neat resin that increased up to ∼6 GPa with up to 7 wt% CNTs incorporated into the polymer matrix has been observed. The axial PNC indentation moduli measured in this work are also over an order of magnitude higher than those of the neat A-CNT arrays measured in prior work (8.9 MPa for 1 vol% A-CNTs, 71.5 MPa for 10 vol% A-CNTs, and 816 MPa for 20 vol% A-CNTs)[11] as a result of full resin infusion here that yields stiff composites compared to the softer A-CNT arrays.

Although the axial moduli do increase with CNT $V_f$, it is observed that even at 30 vol% CNTs, they are still less than estimates *via* rule of mixtures (> 100 GPa for 1 TPa stiffness CNT walls)[63] due to CNT waviness ($w$) governing mechanical behavior, which can reduce the effective elastic axial modulus of long-fiber reinforced composites, including A-CNT arrays, by several orders of magnitude.[8,9,11,12,15,61] This highlights the importance of CNT waviness and alignment direction that govern the resulting mechanical properties, as CNTs that are oriented either parallel[64] or perpendicular[65] to the film direction can exhibit different tensile or compressive behaviors, respectively, with the highest mechanical properties observed in the tensile direction for composites with uniform CNT distribution and high alignment in the film direction.[64] Further, due to the wavy CNTs, the compressive vs. tensile behavior (including to failure) may be different in these nanocomposites compared to traditional aligned microfiber composites, and this will be explored in future work with scaled specimens, discussed in the next section on scaling. To describe the wavy morphology of CNTs, prior work assumed a sinusoidal functional form characterized by the ratio of the amplitude and wavelength of the sine waves, termed the waviness ratio $w$, and showed that

CNT waviness is significant with $w \gtrapprox 0.2$ for as-grown A-CNT arrays.[9,12,15] In addition, this axial indentation modulus scales non-linearly with CNT $V_f$ in both PNCs, similar to the non-linear scaling of the axial indentation modulus with increasing CNT $V_f$ that was previously observed for A-CNT arrays[11] and A-CNT/epoxy PNCs measured up to 20 vol%.[12,15,61] This was attributed to $w$ decreasing at increasing CNT $V_f$ by up to a factor of 2[8,9,61] (consistent with Raman spectroscopy results discussed in Section S4 in the Supporting Information) during the biaxial mechanical densification process, thereby yielding a higher contribution of stiff longitudinal CNT reinforcement to the PNC mechanical behavior with high CNT $V_f$.

To more accurately describe the scaling of axial indentation moduli that accounts for CNT waviness in the PNCs tested here, a previously developed simulation framework[9,61] for PNCs with $10^4$ CNTs within the matrix is applied to this nanoindentation analysis. This model simulated the evolution of $w$ with CNT $V_f$ to evaluate the scaling of the effective CNT elastic modulus with $w$ by incorporating the extension, shear, and bending contributions to the effective CNT compliance in the A-CNT PNC.[9,61] For this nanoindentation analysis, the reinforcement modulus of the CNTs ($E_{cnt}$)[8,9] at various $V_f$s is determined using the simulation technique and used in the axial rule-of-mixtures formula,[9,61] along with $w$ and the polymer matrix elastic modulus ($E_m$), to estimate the composite elastic modulus, $E_{pnc}(V_f)$:

$$E_{pnc}(V_f) = E_{cnt}(w(V_f))V_f + E_m(1 - V_f) \tag{5}$$

The waviness of the A-CNT arrays as a function of $V_f$ ($\rightarrow w(V_f)$) was evaluated from SEM images of the cross-sectional morphology of A-CNT arrays using a sinusoidal amplitude-wavelength definition of $w$.[8,29] This previous study found that CNT confinement causes $w$ to decrease significantly from $\approx 0.20 \pm 0.02$ at $V_f \approx 1\%$ CNTs to $\approx 0.10 \pm 0.01$ at $V_f \approx 20\%$ CNTs, and the following scaling relation for $w(V_f)$ was reported:[8,9,29]

$$w(V_f) = \Lambda(a_1(V_f)^{b_1} + c_1 \pm (a_2(V_f)^{b_2} + c_2)/\sqrt{n}) \tag{6}$$

where $a_1 = -0.04967$, $b_1 = 0.3646$, $c_1 = 0.2489$ (coefficient of determination $\mathbb{R}^2 = 0.9996$); $a_2 = -0.0852$, $b_2 = 0.2037$, $c_2 = 0.2100$ ($\mathbb{R}^2 = 0.9812$); $n = 30$ CNTs;[8,9] and $\Lambda$ is a morphology scaling factor (here $1.2 \pm 0.2$) used to best fit the data. To adjust for variations of CNT morphology arising from slight changes in synthesis conditions from prior work, $\Lambda$ was evaluated to be $\sim 1.2 \pm 0.2$ here and is of similar order of magnitude to previously studied A-CNT PNCs.[9,61] For these PNCs, $\Lambda$ yields a $w$ of $0.24 \pm 0.04$ at 1 vol% CNTs that decreases to $0.12 \pm 0.02$ at 20 vol% CNTs in the PNC matrix. This is consistent with previous work that estimated $w = 0.185 \pm 0.1$ for 18 vol% CNT-epoxy PNCs *via* SEM images that was then input into a finite element model to determine the wavy (effective) CNT modulus.[12,15] Since $w$ was not directly measured for the CNTs in this study, but they are similar to those in our prior work,[8,9,29] a previous modeling and simulation approach[9,61] is used to explain the mechanical property evolution with CNT $V_f$ and waviness. The prediction curves for axial indentation moduli using this simulation are shown in Figure 8 along with the experimental moduli, where these predictions are observed to accurately describe the non-linear scaling of the axial indentation modulus for both the CNT-BMI and CNT-epoxy PNCs, consistent with prior results of stochastic aligned nanofiber systems.[8,9,11,12,15,61] These results highlight the importance of accounting for the observed wavy CNT morphology when quantifying and predicting accurate mechanical behavior scaling, particularly to inform the design of tunable CNT-based composites with enhanced anisotropic mechanical properties.

## Scaling to Bulk Nanocomposite Laminates with High CNT Volume Fractions

Finally, a novel bulk nanocomposite laminating (BNL) process is developed for the scaled production of tough and strong long A-CNT-reinforced PNCs forming individual composite layers and laminates, leveraging the process optimization discussed in the previous sections. The BNL process, as shown in Figure 9 (see Methods), is demonstrated here at the 5 cm-scale to create single plies and then multi-layer unidirectional laminates with two and eight plies

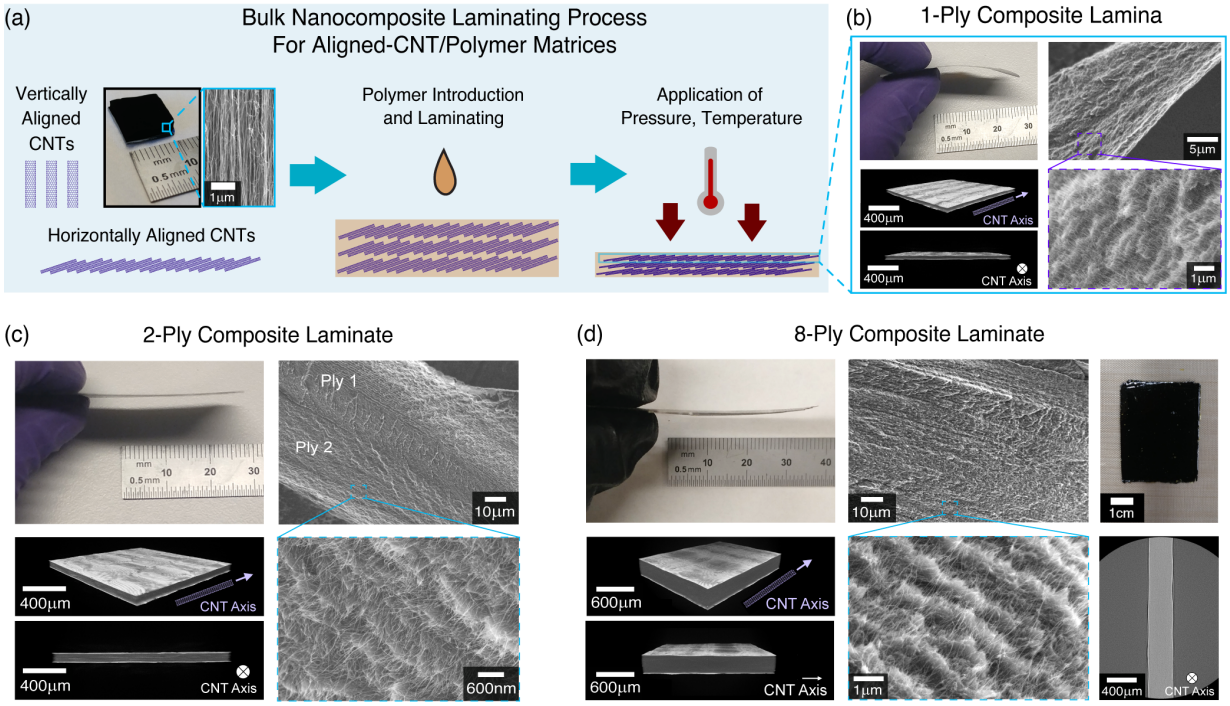


Figure 9: Bulk nanocomposite lamination (BNL) process to create densified aligned CNT-polymer composite laminates. (a) Illustration showing the BNL process where vertically aligned CNT arrays are synthesized, knocked down to induce horizontal alignment, laminated and infused with a polymer matrix, and subjected to additional pressure and temperature to form the final ply and laminate composites, here achieving ∼13 vol% aligned CNTs in a BMI matrix. Optical micrographs, SEM images, and X-ray μCT images show successful BNL composite fabrication, where full polymer infusion, uniform density, thorough CNT-BMI wetting, no microvoids, and consistent CNT alignment and dispersion are achieved for (b) 1-ply lamina, (c) 2-ply laminate, and (d) 8-ply laminate.

of the high-$T_g$ aerospace-grade BMI resin infused into densely packed horizontally aligned CNTs. Here, vertically aligned CNT arrays are synthesized, knocked down mechanically with a rod to induce horizontal alignment,[66] laminated and infused with a polymer based on the high vol% infusion capabilities shown previously in this work, and then subjected to additional pressure and temperature to form the ply and laminate composites, achieving ∼13 vol% aligned CNTs in BMI (see Section S2 in the Supporting Information for TGA curves indicating maintained thermal stability and CNT wt%). Optical micrographs, SEM images, and X-ray μCT images show successful BNL composite fabrication in this scaling demonstration, where full polymer infusion, uniform density, thorough CNT-BMI wetting,

no microvoids, and consistent CNT alignment and dispersion are achieved for a 1-ply lamina (Figure 9b), 2-ply laminate (Figure 9c), and 8-ply laminate (Figure 9d), with a ply thickness of ∼45 μm. The laminates are void-free at the micron scale and fully infused with BMI with high volume fractions of A-CNTs, demonstrating a new platform for creating tough and strong long nanofiber-reinforced bulk composites towards extreme volume fractions and nanofiber lengths. The scale of these BNL laminates can allow for more traditional mechanical testing, including tension and compression to failure, and toughness, among others for both the ply (nanocomposite) and laminates based on the nanocomposite plies.

# Conclusions

In summary, process development leading to the first successful fabrication of fully infused, microvoid-free BMI and epoxy polymer nanocomposites (PNCs) with high volume fractions of biaxially mechanically densified mm-tall aligned carbon nanotube (A-CNT) array reinforcement (1 to 30 vol%, corresponding to inter-CNT spacings of ∼70 to 6 nm) is presented for high-performance structural composite applications. A polymer infusion model developed from Darcy's law accurately predicts the time for resin to infuse into CNT arrays during capillary-assisted PNC processing, corroborated by experimental observations *via* X-ray micro-computed tomography and scanning electron microscopy that a diluted resin with ∼10 × lower viscosity than neat resin is required to obtain complete infusion into high CNT $V_f$ A-CNT arrays (10−30 vol%). For each tested A-CNT vol%, the cured PNCs maintain vertical CNT alignment and glass transition temperature, and the decomposition onset temperature remains constant for epoxy PNCs but increases by ∼8°C for 30 vol% A-CNT BMI PNCs compared to the neat resin. Quasi-static nanoindentation yields a ∼2 × increase in the axial indentation modulus for 30 vol% A-CNT PNCs compared to neat resin and no change in transverse A-CNT modulus, showing enhanced anisotropic mechanical properties with higher CNT $V_f$. In this work, composite processing (*e.g.* successful full

infusion of the nanocomposites at increasing A-CNT vol%) results in a consistent matrix degree of cure, amorphous polymer structure, and vertical CNT alignment in the composite, which correlates with improved mechanical performance over the neat matrix *via* increased axial indentation moduli as a function of A-CNT reinforcement up to 30 vol%. Application to scaled-up bulk nanocomposite laminates is demonstrated, highlighting the potential for further optimization and scaled production of densely packed A-CNT composites and other nanoengineered hybrid materials with advantaged properties.

Building on the work here, the additional component for tailoring these nanocomposites lies with tailoring the interface between the CNT 'fibers' and the polymer matrix, *via* chemical or physical functionalization of the CNT surface, known as sizing in microfiber composites. Conformal polymer deposition techniques and in situ polymerization are some options for interface tailoring with a limited number of polymers. CNT-polymer interfaces, particularly at higher levels of CNT confinement, should also be studied experimentally and *via* ongoing molecular modeling to further understand their evolution with various processing techniques. To supplement the TEM imaging in this study, 3D TEM and X-ray nano-computed tomography could also be employed to image the cross-sections and 3D bulk view of these composites at the nanoscale to investigate the degree of nano-porosity that may or may not be present as a function of CNT $V_f$, as this imaging could be performed at 50 nm resolution or even at 10 nm resolution, potentially leveraging 4D imaging to study process-structure relations. With the capability to fabricate fully infused high density CNT composites beyond 20 vol%, multifunctional property testing could also now be explored, such as electrical conductivity, thermal conductivity, sensing capabilities towards structural health monitoring applications, and CNT nanostitch architectures for interlaminar reinforcement in aerospace laminates and other polymer systems such as thermoplastics, where the formation of a polymer interphase may be more likely to occur to study nano-scale confinement and scale composite performance. In these highly loaded composites that can now be made towards larger scales, tensile (such as DMA) and compression mechanical tests,

including failure, FTIR, and TGA in air can be explored to understand laminate-scale mechanical reinforcement and oxidation resistance for high-performance structural composite applications. Future work should explore these topics and processing methods, especially to determine which yields the composites with the ideal combination of physical properties. This knowledge gained will continue to support the integration of densely packed CNTs for a wide range of applications, such as aerospace polymer composite laminates and nano-engineered hybrid materials with multifunctional properties.

# Methods

## CNT growth and densification to high volume fractions (1−30 vol%)

Vertically aligned CNT arrays with heights of 2 mm (for 1−20 vol% A-CNT PNCs) and 1 mm (for 30 vol% A-CNT PNCs) were synthesized in a 22 mm internal size quartz tube furnace *via* a previously described thermal catalytic chemical vapor deposition (CVD) process, which uses ethylene as the carbon source and water vapor added to inert He gas.[54,66,67] The CNTs were grown on 1 cm × 1 cm Si wafer substrates *via* a base-growth mechanism on a catalyst layer, which is composed of 1 nm Fe on 10 nm $Al_2O_3$ deposited *via* electron beam physical vapor deposition.[17] During growth, the CNTs self-assemble into vertically aligned arrays composed of multiwall CNTs with an average outer diameter of ∼9 nm ($3-7$ walls with ∼5 nm inner diameter and intrinsic CNT density of ≈1.6 g/cm$^3$),[17,66,68] inter-CNT spacing of ∼60−80 nm,[22,29] and CNT $V_f$ of ∼1 vol% CNTs.[29,66] A post-growth 4-min $H_2$ thermal treatment[69] is used to weaken the CNT-catalyst attachment, which allows for easy delamination of the CNT array from the Si substrate using a razor blade, thereby enabling A-CNT array processing in a free-standing state.

A-CNT array samples were then densified *via* a biaxial mechanical densification process.[7,28] A free-standing as-grown A-CNT array was placed in a device made of Teflon and using steel compression rods that permits biaxial compression (densification) in two orthog-

onal directions,[7,10,12] with the final CNT $V_f$ calculated as the ratio of the initial CNT array area to the densified CNT array area.[7,62] The CNT $V_f$ will range from 1 vol% to 5 vol%, 10 vol%, 20 vol%, and 30 vol% with inter-CNT spacings of ~70 to 6 nm,[22,29] corresponding to square array dimensions of ~1.0 $cm^2$ and 1.82 $mm^2$, respectively.[62] See Section S1 in the Supporting Information for additional details.

## Fabrication of A-CNT PNCs *via* capillary-driven infusion and curing of BMI and epoxy resins

To fabricate A-CNT PNCs from two aerospace-grade resins (CYCOM 977-3 epoxy resin and CYCOM 5250-4 BMI resin from Solvay), a free-standing CNT array with 1− 30 vol% CNT $V_f$ was first placed in a steel mold matching its dimensions so that the longitudinal axis of the CNTs was orthogonal to the plane of the mold. Before adding CNTs, the mold was first coated in mold release (Loctite Frekote 700-NC). Then, uncured liquid prepolymers (the unmodified epoxy and BMI resins) were heated to 100°C in glass beakers for degassing in a vacuum oven (1 h for BMI, and 5 h for epoxy). The neat resins were then heated to 120°C for infusion, and they were poured into the 1 vol% and 5 vol% molds to create low-CNT $V_f$ PNCs with each type of polymer matrix, where resin infusion into the A-CNTs occurred for 2 h at 120°C under vacuum. For high-CNT $V_f$ PNCs, 65 wt% resin solutions were made by sonicating the uncured resins in acetone at room temperature for 30 min, and then these solutions were poured into the 10−30 vol% molds for up to 3 h of capillary-assisted infusion at room temperature. After infusion, the PNCs were dried to remove acetone at 80°C for 2 h under vacuum.[36] Additional details can be found in Section S2 in the Supporting Information.

To obtain the final cured PNC samples for each CNT $V_f$, the infused A-CNT arrays were cured following the manufacturer's cure cycles (177°C for 6 h for the epoxy and 177°C for 6 h, plus a 227°C postcure for 6 h for the BMI). To fabricate A-CNT PNCs using the bulk nanocomposite laminating (BNL) method, 500 micron-tall vertically aligned CNT arrays

were synthesized by the CVD process described above on 3x4 cm catalytic Si wafer substrates. To create a one-ply BNL lamina PNC, an as-grown A-CNT array was re-oriented to horizontal alignment *via* densification using a 2 mm diameter rod and Guaranteed Non-porous Teflon (GNPT) film. This was done by placing the film on top of the array and pressing by hand along the long axis (4 cm direction) of the wafer to knock down the A-CNTs into a thin layer.[66] Because the post-growth $H_2$ treatment weakens the attachment of the CNTs to the catalyst, the A-CNTs adhere to the GNPT film and are cleanly removed from the wafer substrate. The 65 wt% diluted BMI solution was then poured onto the layer, and resin infusion and drying was performed as described above. The one-ply CNT-BMI BNL PNC was then cured following the cure and postcure cycle at 0.6 psi to keep the PNC flat, and then it was removed from the GNPT. To create a two-ply BNL laminate PNC, one 3x4 cm A-CNT array was first knocked down on GNPT, and then a second 3x4cm A-CNT array was knocked down on top of it with the same horizontal alignment (unidirectional lay-up), creating a two-ply A-CNT film on GNPT. This was then infused with the diluted BMI solution and cured following the same procedure as the one-ply. To create an eight-ply BNL laminate PNC, four two-ply laminates were infused with resin and then dried as described above. Then, they were removed from the GNPT, stacked on top of one another with the same horizontal alignment (unidirectional lay-up), and placed in a hot press between two GNPT layers to cure at 4.52 MPa following the above cure cycle. The pressure was removed for the post cure. Once cured, all BNL composites were removed from the GNPT film for testing.

## SEM, X-ray μCT, and XRD characterization

High resolution SEM was used to image PNCs that were hand-fractured mechanically along the CNT axis at room temperature by using a razor blade. SEM was performed using a Zeiss Merlin SEM with a 5 mm working distance and 5 kV accelerating voltage. X-ray μCT scans were conducted on the cured PNC samples and cured neat resin using a Zeiss Xradia

520 Versa X-ray microscope with source voltage of 60 kV. 1601 radiograph projections were acquired at a 2 μm isotropic voxel size (∼4-5 μm resolution) with a 3 s exposure time with each sample centered in the field of view (4 mm x 4 mm x 4 mm). Analysis of the 3D volumes was performed using the Zeiss Reconstructor Scout-and-Scan™ Software and Dragonfly™ 4.1 program. A PANalytical X'Pert Pro XRD system in Bragg Brentano geometry was used to analyze the multi-scale structure evolution of the A-CNT array, cured neat epoxy and BMI, and cured PNC samples (not fractured). To probe different structural features, the vertical A-CNT axis was oriented orthogonal and then parallel to the XRD stage by placing the PNCs on their side (rotating 90°) when moving from the orthogonal test to the parallel test. The $2\theta$ angle ranged from 0° to 90°, and Cu K$\alpha$ radiation was passed through a 2° anti-scattering slit with a 0.04 rad soller slit in X'celerator mode. The XRD experiments were performed at 45 kV and 40 mA with a scanning step interval of 0.02° ($2\theta$). $LaB_6$ was used as the standard material for all measurements.

## TGA, DSC, and nanoindentation characterization

DSC and TGA testing for the neat resins, as-grown A-CNTs, and PNC samples were performed with TA Instruments Discovery DSC and TGA systems (Discovery TGA TGA1-0075 and Discovery DSC RCS1-3277 using the TA Instruments™ TRIOS Software v4.4.1 for $T_g$ calculations). For DSC tests, approximately 5 mg of the interior of a sample was placed in a sealed hermetic aluminum DSC pan with a pinhole in the lid, and each test was run from 40°C to 380°C in nitrogen at a ramp rate of 10°C/min in three heat-cool cycles to measure the heat flow into and out of the cured PNC samples at each CNT $V_f$, as well as the cured and uncured resin. Baseline samples (uncured and cured neat polymers) were also tested for comparison purposes, and at least 3 samples of each type were tested. For TGA testing, approximately 2 mg of the interior of a sample was placed in an open high temperature platinum pan and heated in a nitrogen atmosphere from room temperature to 900°C (to ensure thermal degradation). TGA tests were run from 40°C to 900°C in nitrogen at a ramp

rate of 10°C/min, and at least 3 samples of each type were tested.

To prepare the cured neat resin and PNCs for nanoindentation, room temperature ultramicrotoming of the samples was performed using a Leica Ultramicrotome to yield smooth surfaces in the axial and transverse CNT directions of the PNCs[52] with sample thickness $> 500$ μm. Then, nanoindentation testing was performed with a Hysitron TI 950 TriboIndenter following the procedure in Ref. 70 by indenting a 7x7 grid on two samples of each type using a diamond Berkovich tip with a radius of curvature of 150 nm.[28] Testing was performed on cured neat BMI, cured neat epoxy, and BMI and epoxy PNC samples in the axial and transverse CNT directions. Force control (up to 10 mN) was applied *via* a trapezoidal load function, yielding an indentation depth of ∼1 μm. This loading function resulted in quasi-static loading, allowed stabilization of the specimen during the hold period, unloaded quasi-statically, and gave a maximum area of indentation of $\gtrsim$20 μm$^2$ and indentation depth of ∼1 μm to minimize noise in measurements.[62] Therefore, this nanoindentation testing engages $\gtrsim$5000 CNTs in the indentation of 1 vol% PNCs, and $\gtrsim$700,000 CNTs in the indentation of 30 vol% PNCs to capture CNT reinforcement effects on the PNC's indentation modulus.

## Acknowledgement

This work was partially supported by Airbus, ANSYS, Embraer, Lockheed Martin, Saab AB, Saertex, and Teijin Carbon America through MIT's Nano-Engineered Composite aerospace STructures (NECST) Consortium, the National Aeronautics and Space Administration (NASA) Space Technology Research Institute (STRI) for Ultra-Strong Composites by Computational Design (US-COMP), grant number NNX17AJ32G, the U. S. Army Research Laboratory and the U. S. Army Research Office through the Institute for Soldier Nanotechnologies (ISN) under contract number W911NF-13-D-0001 and Cooperative Agreement Number W911NF-18-2-0048, and the U.S. Army Research Office under contract W911NF-07-D-0004. Micro-

computed tomography instrumentation support by the Office of Naval Research (ONR) under the grant number ONR.N000141712068 through the Defense University Research Instrumentation Program (DURIP) is gratefully acknowledged, as well as the material donation of two resins to US-COMP by Solvay that supported this work. A.L.K. was supported by the Department of Defense (DoD) through the National Defense Science and Engineering Graduate Fellowship (NDSEG) Program and gratefully acknowledges Prof. G. Odegard (MTU), Prof. C. Thompson (MIT), Prof. L. Gibson (MIT), and the members of necstlab for technical support and helpful discussions. C.A.C.C. was supported by a 2020-2021 and a 2021-2022 MathWorks Engineering Fellowship at MIT. This work made use of the MIT MRSEC Shared Experimental Facilities supported by the National Science Foundation under award number DMR-0819762, and was carried out in part through the use of MIT's Microsystems Technology Laboratories.

## Supporting Information Available

Supporting Information Available: CNT densification procedure and polymer infusion model details (eqns S1−S24 and Tables S1−S3); CNT PNC fabrication details including resin viscosity measurements for infusion, TGA and DSC analysis of baseline samples, and TGA curves for 1-, 2-, and 8-ply CNT PNC laminates made *via* the BNL process (Figs. S1−S3 and Tables S4 and S5); morphology characterization of CNT PNCs *via* bulk X-ray μCT and cross-sectional SEM, and TEM imaging (Figs. S4−S7); Raman spectroscopy analysis of CNT PNCs including Raman spectra and Raman shifts of the D-, G-, and 2D bands (Fig. S8); and nanoindentation analysis of CNT PNC mechanical properties including representative nanoindentation curves and moduli data sets (Fig. S9 and Tables S6 and S7).

# References


1. De Volder, M. F. L.; Tawfick, S. H.; Baughman, R. H.; Hart, A. J. Carbon Nanotubes: Present and Future Commercial Applications. *Science* **2013**, *339*, 535–539.

2. Rao, R.; Pint, C. L.; Islam, A. E.; Weatherup, R. S.; Hofmann, S.; Meshot, E. R.; Wu, F.; Zhou, C.; Dee, N.; Amama, P. B.; Carpena-Nuñez, J.; Shi, W.; Plata, D. L.; Penev, E. S.; Yakobson, B. I.; Balbuena, P. B.; Bichara, C.; Futaba, D. N.; Noda, S.; Shin, H.; Kim, K. S.; Simard, B.; Mirri, F.; Pasquali, M.; Fornasiero, F.; Kauppinen, E. I.; Arnold, M.; Cola, B. A.; Nikolaev, P.; Arepalli, S.; Cheng, H.-M.; Zakharov, D. N.; Stach, E. A.; Zhang, J.; Wei, F.; Terrones, M.; Geohegan, D. B.; Maruyama, B.; Maruyama, S.; Li, Y.; Adams, W. W.; Hart, A. J. Carbon Nanotubes and Related Nanomaterials: Critical Advances and Challenges for Synthesis toward Mainstream Commercial Applications. *ACS Nano* **2018**, *12*, 11756–11784.

3. Sun, H.; Zhang, Y.; Zhang, J.; Sun, X.; Peng, H. Energy harvesting and storage in 1D devices. *Nat. Rev. Mater.* **2017**, *2*, 17023.

4. Zhong, D.; Zhang, Z.; Ding, L.; Han, J.; Xiao, M.; Si, J.; Xu, L.; Qiu, C.; Peng, L.-M. Gigahertz integrated circuits based on carbon nanotube films. *Nature Electronics* **2018**, *1*, 40–45.

5. Xu, Q.; Li, W.; Ding, L.; Yang, W.; Xiao, H.; Ong, W.-J. Function-driven engineering of 1D carbon nanotubes and 0D carbon dots: mechanism, properties and applications. *Nanoscale* **2019**, *11*, 1475–1504.

6. Zhang, Y.; Heo, Y.-J.; Son, Y.-R.; In, I.; An, K.-H.; Kim, B.-J.; Park, S.-J. Recent advanced thermal interfacial materials: A review of conducting mechanisms and parameters of carbon materials. *Carbon* **2019**, *142*, 445 – 460.

7. Wardle, B. L.; Saito, D. S.; García, E. J.; Hart, A. J.; Guzmán de Villoria, R.; Ver-

ploegen, E. A. Fabrication and Characterization of Ultrahigh-Volume- Fraction Aligned Carbon Nanotube Polymer Composites. *Adv. Mater.* **2008**, *20*, 2707–2714.

8. Stein, I. Y.; Lewis, D. J.; Wardle, B. L. Aligned Carbon Nanotube Array Stiffness from Stochastic Three-dimensional Morphology. *Nanoscale* **2015**, *7*, 19426–19431.

9. Stein, I. Y.; Wardle, B. L. Mechanics of Aligned Carbon Nanotube Polymer Matrix Nanocomposites Simulated via Stochastic Three-dimensional Morphology. *Nanotechnology* **2016**, *27*, 035701.

10. Marconnet, A. M.; Yamamoto, N.; Panzer, M. A.; Wardle, B. L.; Goodson, K. E. Thermal Conduction in Aligned Carbon Nanotube Polymer Nanocomposites with High Packing Density. *ACS Nano* **2011**, *5*, 4818–4825.

11. Cebeci, H.; Stein, I. Y.; Wardle, B. L. Effect of nanofiber proximity on the mechanical behavior of high volume fraction aligned carbon nanotube arrays. *Appl. Phys. Lett.* **2014**, *104*, 023117.

12. Cebeci, H.; Guzmán de Villoria, R.; Hart, A. J.; Wardle, B. L. Multifunctional properties of high volume fraction aligned carbon nanotube polymer composites with controlled morphology. *Compos. Sci. Technol.* **2009**, *69*, 2649–2656.

13. Liu, L.; Corma, A. Metal Catalysts for Heterogeneous Catalysis: From Single Atoms to Nanoclusters and Nanoparticles. *Chem. Rev.* **2018**, *118*, 4981–5079.

14. Kirmani, M. H.; Ramachandran, J.; Arias-Monje, P. J.; Gulgunje, P.; Kumar, S. The effects of processing and carbon nanotube type on the impact strength of aerospace-grade bismaleimide based nanocomposites. *Polym Eng Sci* **2022**, *62*, 1187–1196.

15. Handlin, D.; Stein, I. Y.; Guzman de Villoria, R.; Cebeci, H.; Parsons, E. M.; Socrate, S.; Scotti, S.; Wardle, B. L. Three-Dimensional Elastic Constitutive Relations of Aligned Carbon Nanotube Architectures. *J. Appl. Phys.* **2013**, *114*, 224310.

16. Dastgerdi, J. N.; Marquis, G.; Salimi, M. Micromechanical modeling of nanocomposites considering debonding and waviness of reinforcements. *Compos. Struct.* **2014**, *110*, 1 – 6.

17. Stein, I. Y.; Wardle, B. L. Morphology and Processing of Aligned Carbon Nanotube Carbon Matrix Nanocomposites. *Carbon* **2014**, *68*, 807 – 813.

18. Chazot, C. A. C.; Hart, A. J. Understanding and control of interactions between carbon nanotubes and polymers for manufacturing of high-performance composite materials. *Composites Science and Technology* **2019**, *183*, 107795.

19. Pisani, W. A.; Radue, M. S.; Patil, S. U.; Odegard, G. M. Interfacial modeling of flattened CNT composites with cyanate ester and PEEK polymers. *Composites Part B: Engineering* **2021**, *211*, 108672.

20. Deshpande, P. P.; Radue, M. S.; Gaikwad, P.; Bamane, S.; Patil, S. U.; Pisani, W. A.; Odegard, G. M. Prediction of the Interfacial Properties of High-Performance Polymers and Flattened CNT-Reinforced Composites Using Molecular Dynamics. *Langmuir* **2021**, *37*, 11526–11534.

21. Winey, K. I.; Vaia, R. A. Polymer Nanocomposites. *MRS Bulletin* **2007**, *32*, 314–322.

22. Stein, I. Y.; Wardle, B. L. Coordination Number Model to Quantify Packing Morphology of Aligned Nanowire Arrays. *Phys. Chem. Chem. Phys.* **2013**, *15*, 4033–4040.

23. Kaiser, A. L.; Nwenyi, J. C.; Wardle, B. L. Process-Structure-Property Characterization of Phenolic Matrix Nanocomposites Reinforced with Dense Aligned Carbon Nanotube Arrays. *AIAA Scitech 2021 Forum* **2021**, 1775.

24. Atescan, Y.; Hadden, C. M.; Wardle, B. L.; Odegard, G. M.; Cebeci, H. Molecular Dynamics and Finite Element Investigation of Polymer Interphase Effects on Effective

Stiffness of Wavy Aligned Carbon Nanotube Composites. *56th AIAA/ASCE/AHS/ASC Structures, Structural Dynamics, and Materials Conference* **2015**,

25. Choi, H. K.; Yu, J.; Kim, E.; Shin, E. S. Estimation of interfacial properties of nanocomposites using an analytical interphase model. *Compos. Struct.* **2018**, *184*, 437 – 442.

26. Pramanik, C.; Nepal, D.; Nathanson, M.; Gissinger, J. R.; Garley, A.; Berry, R. J.; Davijani, A.; Kumar, S.; Heinz, H. Molecular engineering of interphases in polymer/carbon nanotube composites to reach the limits of mechanical performance. *Compos. Sci. Technol.* **2018**, *166*, 86 – 94.

27. Patil, S. U.; Radue, M. S.; Pisani, W. A.; Deshpande, P.; Xu, H.; Al Mahmud, H.; Dumitrică, T.; Odegard, G. M. Interfacial characteristics between flattened CNT stacks and polyimides: A molecular dynamics study. *Computational Materials Science* **2020**, *185*, 109970.

28. Kaiser, A. L. Interfacial and physical confinement effects on the structure and properties of aligned carbon nanotube architectures. Ph.D. thesis, Massachusetts Institute of Technology, 2021.

29. Stein, I. Y.; Wardle, B. L. Packing morphology of wavy nanofiber arrays. *Phys. Chem. Chem. Phys.* **2016**, *18*, 694.

30. Kaiser, A. L.; Lidston, D.; Peterson, S. C.; Acauan, L.; Steiner III, S.; Guzman de Villoria, R.; Vanderhout, A. R.; Stein, I. Y.; Wardle, B. L. Substrate adhesion evolves non-monotonically with processing time in millimeter-scale aligned carbon nanotube arrays. *Nanoscale* **2021**, *13*, 261.

31. Wang, S.; Haldane, D.; Liang, R.; Smithyman, J.; Zhang, C.; Wang, B. Nanoscale infiltration behaviour and through-thickness permeability of carbon nanotube buckypapers. *Nanotechnology* **2012**, *24*, 015704.

32. Wang, Z.; Liang, Z.; Wang, B.; Zhang, C.; Kramer, L. Processing and property investigation of single-walled carbon nanotube (SWNT) buckypaper/epoxy resin matrix nanocomposites. *Composites Part A: Applied Science and Manufacturing* **2004**, *35*, 1225–1232.

33. Tomadakis, M. M.; Sotirchos, S. V. Knudsen diffusivities and properties of structures of unidirectional fibers. *AIChE J.* **1991**, *37*, 1175–1186.

34. Downes, R. D.; Hao, A.; Park, J. G.; Su, Y.-F.; Liang, R.; Jensen, B. D.; Siochi, E. J.; Wise, K. E. Geometrically constrained self-assembly and crystal packing of flattened and aligned carbon nanotubes. *Carbon* **2015**, *93*, 953–966.

35. Tomadakis, M. M.; Robertson, T. J. Viscous Permeability of Random Fiber Structures: Comparison of Electrical and Diffusional Estimates with Experimental and Analytical Results. *Journal of Composite Materials* **2005**, *39*, 163–188.

36. Cheng, Q.; Wang, B.; Zhang, C.; Liang, Z. Functionalized Carbon-Nanotube Sheet/Bismaleimide Nanocomposites: Mechanical and Electrical Performance Beyond Carbon-Fiber Composites. *Small* **2010**, *6*, 763–767.

37. Garcea, S. C.; Wang, Y.; Withers, P. J. X-ray computed tomography of polymer composites. *Composites Science and Technology* **2018**, *156*, 305–319.

38. Gu, A.; Liang, G.; Liang, D.; Ni, M. Bismaleimide/carbon nanotube hybrids for potential aerospace application: I. Static and dynamic mechanical properties. *Polym. Adv. Technol.* **2007**, *18*, 835–840.

39. Chandran M., S.; Krishna, M.; Salini, K.; Rai, K. S. Preparation and Characterization of Chain-Extended Bismaleimide/Carbon Fibre Composites. *Int. J. Poly. Sci.* **2010**, *2010*.

40. Kirmani, M. H.; Gulgunje, P.; Ramachandran, J.; Arias-Monje, P. J.; Wang, P.-H.; Kumar, S. Learning from Nature: Molecular Rearrangement in the Bismaleimide System

Leading to Dramatic Increase in Impact Strength. *ACS Appl. Polym. Mater.* **2020**, *2*, 758–767.

41. Shen, J.; Huang, W.; Wu, L.; Hu, Y.; Ye, M. Thermo-physical properties of epoxy nanocomposites reinforced with amino-functionalized multi-walled carbon nanotubes. *Composites Part A: Applied Science and Manufacturing* **2007**, *38*, 1331 – 1336.

42. Surana, R.; Pyne, A.; Rani, M.; Suryanarayanan, R. Measurement of enthalpic relaxation by differential scanning calorimetry–effect of experimental conditions. *Thermochimica Acta* **2005**, *433*, 173–182.

43. Kirmani, M. H.; Sachdeva, G.; Pandey, R.; Odegard, G. M.; Liang, R.; Kumar, S. Cure Behavior Changes and Compression of Carbon Nanotubes in Aerospace Grade Bismaleimide-Carbon Nanotube Sheet Nanocomposites. *ACS Appl. Nano Mater.* **2021**, *4*, 2476–2485.

44. Huang, W.; Wang, Y.; Luo, G.; Wei, F. 99.9nanotubes by vacuum high-temperature annealing. *Carbon* **2003**, *41*, 2585–2590.

45. Park, S.-J.; Chae, S.-W.; Rhee, J.-M.; Kang, S.-J. A Study on Electrical and Thermal Properties of Polyimide/MWNT Nanocomposites. *Korean Chem. Soc* **2010**, *31*.

46. Liu, L.; Gu, A.; Fang, Z.; Tong, L.; Xu, Z. The effects of the variations of carbon nanotubes on the micro-tribological behavior of carbon nanotubes/bismaleimide nanocomposite. *Composites, Part A* **2007**, *38*, 1957–1964.

47. Liu, J.; Chen, C.; Feng, Y.; Liao, Y.; Ye, Y.; Xie, X.; Mai, Y.-W. Ultralow-Carbon Nanotube-Toughened Epoxy: The Critical Role of a Double-Layer Interface. *ACS Appl. Mater. Interfaces* **2018**, *10*, 1204–1216.

48. Montazeri, A.; Madah, D.; Shormasti, N. K. The comparison of cure behavior of epoxy

and multi-wall carbon nanotube/epoxy composites. *J. Therm. Anal. Calorim.* **2016**, *124*, 1441–1448.

49. Xie, H.; Liu, B.; Sun, Q.; Yuan, Z.; Shen, J.; Cheng, R. Cure kinetic study of carbon nanofibers-epoxy composites by isothermal DSC. *J. Appl. Polym. Sci.* **2005**, *96*, 329–335.

50. Cheng, Q.; Wang, J.; Jiang, K.; Li, Q.; Fan, S. Fabrication and properties of aligned multiwalled carbon nanotube-reinforced epoxy composites. *Journal of Materials Research* **2008**, *23*, 2975–2983.

51. Gair, J. L., Jr.; Lidston, D. L.; Cole, D. P.; Lambeth, R. H.; Hsieh, A. J.; Bruck, H. A.; Hall, A. J.; Bundy, M. L.; Wardle, B. L. Ultrahigh Carbon Nanotube Volume Fraction Effects on Micromechanical Quasi-Static & Dynamic Properties of Poly(Urethane-Urea) Filled Nanocomposites. *Multidisciplinary Digital Publishing Institute (MDPI) Proceedings* **2018**, *2*, 398.

52. Gair, J. L.; Lambeth, R. H.; Cole, D. P.; Lidston, D. L.; Stein, I. Y.; Kalfon-Cohen, E.; Hsieh, A. J.; Bruck, H. A.; Bundy, M. L.; Wardle, B. L. Strong process-structure interaction in stoveable poly(urethane-urea) aligned carbon nanotube nanocomposites. *Compos. Sci. Technol.* **2018**, *166*, 115 – 124.

53. Kalfon-Cohen, E.; Kopp, R.; Furtado, C.; Ni, X.; Arteiro, A.; Borstnar, G.; Mavrogordato, M. N.; Sinclair, I.; Spearing, S. M.; Camanho, P. P.; Wardle, B. L. Synergetic effects of thin plies and aligned carbon nanotube interlaminar reinforcement in composite laminates. *Compos. Sci. Technol.* **2018**, *166*, 160–168.

54. Stein, I. Y.; Kaiser, A. L.; Constable, A. J.; Acauan, L.; Wardle, B. L. Mesoscale evolution of non-graphitizing pyrolytic carbon in aligned carbon nanotube carbon matrix nanocomposites. *J. Mater. Sci.* **2017**, *52*, 13799–13811.

55. Dhanapal, D.; Muthukaruppan, A.; Srinivasan, A. K. Tetraglycidyl Epoxy Reinforced with Surface Functionalized Mullite Fiber for Substantial Enhancement in Thermal and Mechanical Properties of Epoxy Nanocomposites. *Silicon* **2018**, *10*, 585–594.

56. Singh, D. K.; Iyer, P.; Giri, P. Diameter Dependence of Interwall Separation and Strain in Multiwalled Carbon Nanotubes Probed by X-Ray Diffraction and Raman Scattering Studies. *Diamond Relat. Mater.* **2010**, *19*, 1281 – 1288.

57. Upadhyaya, P.; Roy, S.; Haque, M. H.; Lu, H. Influence of nano-clay compounding on thermo-oxidative stability and mechanical properties of a thermoset polymer system. *Composites Science and Technology* **2013**, *84*, 8–14.

58. Zhang, Y.; Chern, D.; Schulz, R.; Mauzeroll, J.; Chromik, R. R. Manufacturing and Tribological Behavior of Self-Lubricating Duplex Composites: Graphite-Reinforced Polymer Composites and Polymer-Infiltrated Metal Networks. *Journal of Materials Engineering and Performance* **2021**, *30*, 103–115.

59. Koumoulos, E. P.; Jagdale, P.; Kartsonakis, I. A.; Giorcelli, M.; Tagliaferro, A.; Charitidis, C. A. Carbon nanotube/polymer nanocomposites: A study on mechanical integrity through nanoindentation. *Polym. Compos.* **2014**, *36*, 1432–1446.

60. Zabet, M.; Moradian, S.; Ranjbar, Z.; Zanganeh, N. Effect of carbon nanotubes on electrical and mechanical properties of multiwalled carbon nanotubes/epoxy coatings. *Journal of Coatings Technology and Research* **2016**, *13*, 191–200.

61. Natarajan, B.; Stein, I. Y.; Lachman, N.; Yamamoto, N.; Jacobs, D. S.; Sharma, R.; Liddle, J. A.; Wardle, B. L. Aligned carbon nanotube morphogenesis predicts physical properties of their polymer nanocomposites. *Nanoscale* **2019**, *11*, 16327–16335.

62. Gair, J. Nanotube-Matrix Interplay and Tunability in Ultrahigh Volume-Fraction Aligned Carbon Nanotube Poly (Urethane-urea) Nanocomposites. Ph.D. thesis, Dept. of Mech. Eng., University of Maryland, 2017.

63. Salvetat, J.-P.; Bonard, J.-M.; Thomson, N. H.; Kulik, A. J.; Forro, L.; Benoit, W.; Zuppiroli, L. Mechanical properties of carbon nanotubes. *Appl. Phys. A* **1999**, *69*, 255–260.

64. Han, Y.; Zhang, X.; Yu, X.; Zhao, J.; Li, S.; Liu, F.; Gao, P.; Zhang, Y.; Zhao, T.; Li, Q. Bio-Inspired Aggregation Control of Carbon Nanotubes for Ultra-Strong Composites. *Scientific Reports* **2015**, *5*, 11533.

65. Li, L.; Yang, Z.; Gao, H.; Zhang, H.; Ren, J.; Sun, X.; Chen, T.; Kia, H. G.; Peng, H. Vertically Aligned and Penetrated Carbon Nanotube/Polymer Composite Film and Promising Electronic Applications. *Adv. Mater.* **2011**, *23*, 3730–3735.

66. Lee, J.; Stein, I. Y.; Devoe, M. E.; Lewis, D. J.; Lachman, N.; Kessler, S. S.; Buschhorn, S. T.; Wardle, B. L. Impact of Carbon Nanotube Length on Electron Transport in Aligned Carbon Nanotube Films. *Appl. Phys. Lett.* **2015**, *106*, 053110.

67. Kaiser, A. L.; Stein, I. Y.; Cui, K.; Wardle, B. L. Process-morphology scaling relations quantify self-organization in capillary densified nanofiber arrays. *Phys. Chem. Chem. Phys.* **2018**, *20*, 3876–3881.

68. Stein, I. Y.; Lachman, N.; Devoe, M. E.; Wardle, B. L. Exohedral Physisorption of Ambient Moisture Scales Non-Monotonically with Fiber Proximity in Aligned Carbon Nanotube Arrays. *ACS Nano* **2014**, *8*, 4591–4599.

69. Mitchell, R. R.; Yamamoto, N.; Cebeci, H.; Wardle, B. L.; Thompson, C. V. A technique for spatially-resolved contact resistance-free electrical conductivity measurements of aligned-carbon nanotube/polymer nanocomposites. *Compos. Sci. Technol.* **2013**, *74*, 205 – 210.

70. Kaiser, A. L.; Acauan, L.; Wardle, B. L. Process-Structure-Property Relations in Dense Aligned Carbon Nanotube/Aerospace-grade Epoxy Nanocomposites. *AIAA Scitech 2022 Forum* **2022**, 1095.